Petroleum Science 22 (2025) 1270–1288

Contents lists available at ScienceDirect

Petroleum Science

journal homepage: www.keaipublishing.com/en/journals/petroleum-science

Original Paper

Mechanism of proppant transport and deposition in rough intersecting fractures after offshore fracturing

Biao Yin [a, b], Yi-Shan Lou [a, b], Shan-Yong Liu [a, b, c], Yan Zhang [a, b, *]

[a] School of Petroleum Engineering, Yangtze University, Wuhan, 430113, Hubei, China
[b] National Engineering Research Center for Oil & Gas Drilling and Completion Technology, Yangtze University, Wuhan, 430100, Hubei, China
[c] Institute of Mud Logging Technology and Engineering, Yangtze University, Jingzhou, 434023, Hubei, China

ARTICLE INFO

Article history:
Received 5 March 2024
Received in revised form
17 January 2025
Accepted 19 January 2025
Available online 21 January 2025

Edited by Jia-Jia Fei

Keywords:
Hydraulic fracturing
Intersecting fracture
Proppant
Turbulent kinetic energy
CFD-DEM
Sphericity
Joint roughness coefficient

ABSTRACT

To accurately analyze proppant transport in rough intersecting fractures and elucidate the interaction mechanisms among liquid, particles, and rough walls, this study reconstructed a numerical model of fractures in inhomogeneous reservoirs with varying brittleness index (BI). Various auto-correlation Gaussian rough fracture models were created using Matlab to assess roughness through the fractal dimension method. This research innovatively combined Boolean operations to establish three-dimensional rough fracture models, incorporating (Computational Fluid Dynamics) CFD-DEM (Discrete Element Method) with a bidirectional method for cosimulation. The proppant transport in fractures was categorized into three zones based on the difference in the turbulent kinetic energy. Artificially induced fracture roughness increases fluid retention and turbulence, causing plugging effects and limiting proppant flow into branch fractures. Additionally, compared with the superior deposition and significant support effects of the spherical proppant, the low-sphericity proppant traveled farther under fracturing fluid, inducing more pronounced plugging near curved fracture intersections; the variation in fracture intersection angles primarily impacted the wall shear stress within the flow field, indicating smaller angles led to higher shear energy at the intersection. Compared with the intersection angle of 30°, the height and area deposited in the 90° branch fracture increased by 52.25% and 65.33%, respectively; notably, injecting proppant from smaller to larger particles (S:M:L) and a low velocity effectively ensured fracture conductivity near the wellbore at joint roughness coefficient (JRC) ≥46 while achieving satisfactory placement in the branch fracture, making it a recommended approach.

1. Introduction

In recent decades, the development of drilling and completion technologies, such as hydraulic fracturing has made the development of conventional reservoirs with low porosity and permeability economically feasible due to the reduction in hydrocarbon reserves. Proppant is an essential substance used in the hydraulic fracturing process to pump fracturing fluid into reservoirs as a carrier to support fractures effectively and form an artificial fracture with long-term conductivity. It mainly includes quartz sand, ceramic granules and resin-clad sand (Wen et al., 2022). Under the influence of closure pressure, the proppant will gradually undergo changes such as embedding, crushing, and deformation, leading to a gradual loss of hydraulic fracture conductivity. Therefore, achieving efficient proppant transport in complex fractures and forming fractures with long-lasting, high conductivity has been a primary objective for relevant researchers.

The transport and distribution of proppant in hydraulic fractures play a key role in determining fracture conductivity within the fractures, attracting many scholars to conduct experimental studies. Kern et al. (1959) were the first to conduct a plate experiment on sand-water mixing transport, which indicated the injected proppant would be deposited at the bottom of the tank to form a dune-like structure, thus proposing a method for calculating the equilibrium height. The STIM-LAB laboratory has studied proppant transport experiments for more than 20 years and has collected much experimental data on plate flow, while experimental results have rarely been published (Patankar et al., 2002). Alotaibi and

* Corresponding author.
E-mail address: yanzhang@yangtzeu.edu.cn (Y. Zhang).

https://doi.org/10.1016/j.petsci.2025.01.008

Miskimins (2015) studied the sand-carrying pattern of slickwater in intersected fractures and proposed a relational equation to predict the height of deposition adapted to different scales. Sievert et al. (1981) employed dynamic sand-carrying experiments to derive empirical formulas for determining the settling velocity of proppant particles in flat fractures. However, owing to variations in experimental equipment, materials, and conditions among researchers, significant discrepancies exist in the resulting empirical formulas.

Plate flow experiments revealed that the proppant was carried by low-viscosity fluids, resulting in the large size of the proppant gradually settling near the wellbore; as the sand bed grew, the proppant gradually reached its equilibrium height and transformed into a dike. Due to the obstruction of the sand dike, the flow of fracturing fluid near the injection is altered, causing the subsequently injected proppant particles to be lifted vertically and carried over the sand dike farther out (Qu et al., 2021, 2023a, 2023b). A schematic diagram of proppant transport in the fracture is shown in Fig. 1, which clearly shows that the transport state of the proppant can be divided into three regions: the region of deposition, the post-injection region, and the upper pure liquid area (Suri et al., 2020; Wang et al., 2003; Sahai et al., 2014). Basiuk et al. (2021) compared the results through qualitative analysis with smooth walls more commonly found in laboratory tests and reported that rough fractures at high pumping rates can significantly increase the amount of proppant deposition. Research on different geological and engineering parameters has been conducted with improvements in experimental conditions and field data (Liu et al., 2024).

To address the specific demands and challenges of offshore environments, smaller displacement and lower viscosity fluids are typically employed in hydraulic fracturing, leading to insufficient fracturing and reduced proppant suspension capabilities. The brittleness index (BI) is a key parameter for characterizing reservoir rock properties and guiding production. In the South China Sea, the BI of offshore inhomogeneous reservoirs varies significantly, with hydraulic fractures often exhibiting different degrees of roughness (Martyushev et al., 2023a). To accurately represent the actual condition of fracture surfaces, Barton derived empirical equations for the peak shear strength of the structural surface inherent in rock through numerous experimental studies since 1973, resulting in the introduction of an important parameter for quantifying the roughness of the surface, namely, the joint roughness coefficient (JRC) (Barton, 1973). Methods for reconstructing rough fractures are primarily divided into two categories: statistical approaches based on fractal theory and digital rock-based techniques (Akhshik and Rajabi, 2022). The former integrates simulation calculations more effectively to address research needs concerning large deformations and nonlinearities; the latter can closely approximate post-fracturing surfaces but encounter convergence issues in simulations. Currently, considering the limitations and costs of experimental conditions, numerical simulation (CFD-DEM) has become another efficient method for evaluating proppant transport and spreading within fractures (Tang et al., 2022; Zhang et al., 2022). The Eulerian-Eulerian and Eulerian-Lagrange models are now commonly applied in solid-liquid calculations. Studies on proppant transport and placement processes in complex rough fractures are often combined with scans of cores, focusing on the optimization of production parameters (Aminnia et al., 2023; Martyushev et al., 2023b; Zhou et al., 2011). However, existing studies have focused almost exclusively on the roughness of specific reservoirs, lacking broader applicability.

There are significant differences in the roughness of post-fracturing fractures in offshore inhomogeneous reservoirs with different BI. Previously, point cloud data of rough fractures were generated by scanning via specific equipment to generate a collection of vectors in a 3D coordinate system, which is expensive and time-consuming and does not couple well with the CFD-DEM simulation process, resulting in nonconvergent simulation results. To solve this problem, Matlab programming was used to obtain autocorrelated Gaussian surfaces to establish numerical models of fractures with different roughnesses. Hereby, the JRC of rough surfaces is innovatively quantified using the box-counting method to determine fractal dimension. A reliable understanding of the process (transport, deposition) within the flow field due to the presence of rough fractures was achieved by incorporating the Euler-Lagrange model in the CFD-DEM. This study addressed a research gap in proppant transport and deposition concerning sphericality, systematically evaluating how the intersection angles of fracture and sequences of proppant injection influence placement processes.

2. Methodology

Fig. 2(a) illustrates the process of CFD-DEM software coupling, while Fig. 2(b) shows a schematic of solid-liquid motion during coupling. The CFD-DEM simulations involve two-way coupling, where pressure and momentum from the fluid are transferred to particles by simultaneously calculating the pressure and velocity fields. Various forces, including contact and Saffman lift forces, act on the particles to update their positions and velocities. The resulting particle reaction forces are then used to update the pressure and velocity fields of the fluid.

To consider the transport patterns of different types of proppant morphologies in intersecting rough fractures, our study examined the transport processes of proppants with three different sphericities using the multispherical construction of aspheric particles. The discrete phase (particles) is considered a collection of individual particles subject to the control of Newton's second law. The continuous phase is set as an incompressible fluid. The change in the position of the particles and the fluid is obtained by updating the coupled calculation of the forces interacting between them (drag force, lift force, pressure gradient force). The specific fluid-

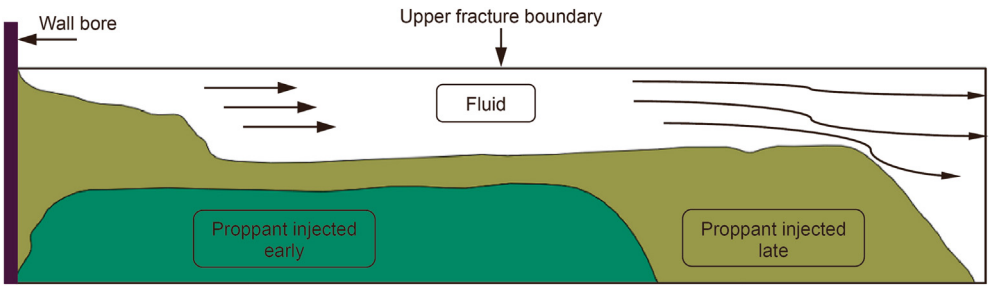

Fig. 1. Schematic diagram of proppant transport in a fracture.

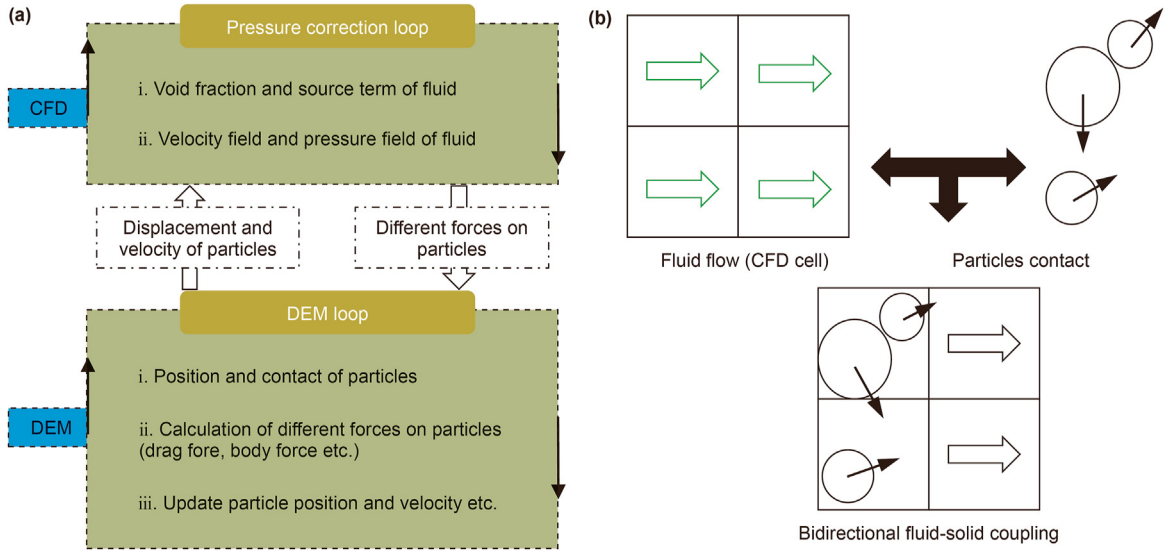

Fig. 2. (**a**) CFD-DEM coupling process (Zeng et al., 2016). (**b**) Schematic diagram of CFD-DEM coupling.

particle phase control equations are as follows.

2.1. Fluid phase

The calculation of the flow field is mainly controlled by locally averaged three-dimensional Navier-Stokes equations with source terms (Opoku et al., 2023). According to the finite volume calculation method, the fluid region is divided into numerous units based on the law of mass conservation. The equation is expressed as:

$$\frac{\partial\left(\alpha\rho_{\mathrm{f}}\right)}{\partial t}+\nabla\cdot\left(\alpha\rho_{\mathrm{f}}\boldsymbol{u}_{\mathrm{f}}\right)=0 \tag{1}$$

where $\boldsymbol{u}_{\mathrm{f}}$ is the fluid velocity, ρ_{f} is the fluid density, α is the volume fraction of the fluid phase and t is time. The conservation of momentum equation is (Dontsov and Peirce, 2014):

$$\frac{\partial\left(\alpha\rho_{\mathrm{f}}\boldsymbol{u}_{\mathrm{f}}\right)}{\partial t}+\nabla\cdot\left(\alpha\rho_{\mathrm{f}}\boldsymbol{u}_{\mathrm{f}}\boldsymbol{u}_{\mathrm{f}}\right)=-\alpha\nabla p+\alpha\nabla\cdot\tau-S_{\mathrm{f}}+\alpha\rho_{\mathrm{f}}\boldsymbol{g} \tag{2}$$

where p is the fluid pressure, τ is the viscous stress tensor, and S_{f} is the average interaction force per unit volume.

The source term S_{f} for a particular computational cell is calculated by summing the fluid interaction forces on all particles within the cell and dividing by the fluid volume of the mesh.

$$S_{\mathrm{f}}=\frac{\left(\sum_{i=1}^{M}\boldsymbol{F}_{\mathrm{f},i}\right)}{V_{\mathrm{cell}}} \tag{3}$$

where M is the number of particles in the cell, $\boldsymbol{F}_{\mathrm{f},i}$ is the fluid force on the particles, and V_{cell} is the volume of fluid in the calculated cell.

2.2. Particle phase

The EDEM is used to simulate particle collisions. We present the equations describing the CFD and DEM input parameters applied to describe the control of motion of the fluid and particle phases. Differences in the morphology (sphericity) of the particles lead to great variations in their transport and deposition processes. The modeling process for irregular particles often presents a combination of rigidly connected spheres, where the model forces and contacts are based on the location of the surface (Kruggel-Emden et al., 2008). To control the study variables, this study establishes the same volume of particles with different shapes as shown in Fig. 3. When the distance between the centers of adjacent proppants equals the sum of their radii, the particles are in contact. Under the premise that all particles have a certain volume and density, we innovatively established three different particle samples (Fig. 4), rod proppant (S1), irregular sub-circular composed of 12 particles (S2) and spherical particles (S3).

Sphericity describes the similarity between particles and spheroids, which is strongly related to transport distance and mineral morphology. The sphericity greatly determines the difference in the way the particles are transported. Particles with high sphericity move in the way of rolling, while particles with low sphericity move in a floating manner. According to China's oil and gas industry standard SY/T5108-1997, the definition of sphericity is:

$$S_{\mathrm{p}}=\frac{d_{\mathrm{n}}}{d_{\mathrm{c}}} \tag{4}$$

where S_{p} is the sphericity of the particle; d_{n} is the sphere diameter of the equivalent volume of the particle; d_{c} is the diameter of the external sphere. By measuring the volume, the sphericity of the three established particles is obtained as shown in Table 1.

According to Newton's second law, the transport of particle p will be subject to gravity, buoyancy, contact forces (particle-

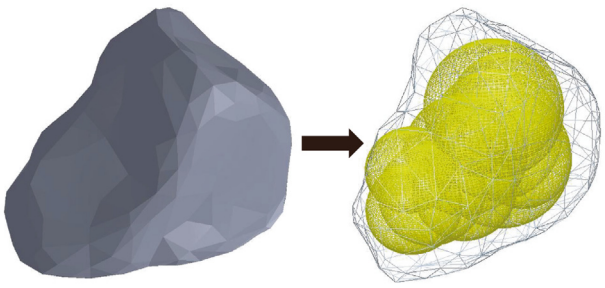

Fig. 3. Modeling of irregular particles.

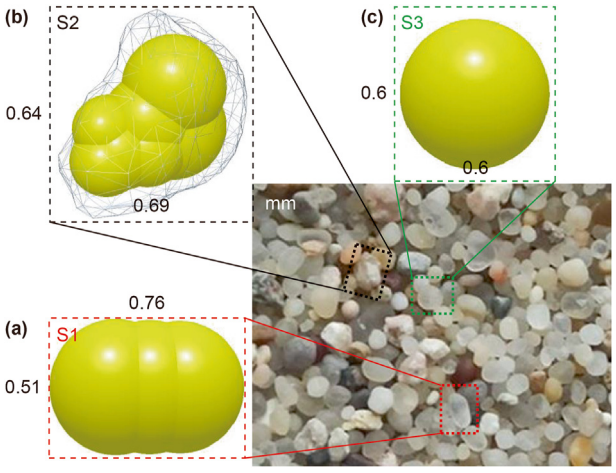

Fig. 4. Model of 3 kinds of particles with different sphericities.

Table 1
Establishment of three distinct proppants and their corresponding sphericities.

Particle	Sphericity
Smooth sphere (S3)	1
Rod-shaped (S1)	0.92
Sub-circular (S2)	0.78

particle, particle-wall), interaction forces (tension forces, wall shear forces, rotational lift forces, etc.) (Wang et al., 2019).

$$m_{\mathrm{p}}\frac{\partial \boldsymbol{u}_{\mathrm{p}}}{\partial t}=m_{\mathrm{p}}\boldsymbol{g}\left(1-\frac{\rho_{\mathrm{f}}}{\rho_{\mathrm{p}}}\right)+\left(\sum_{i=1}^{k_{\mathrm{c}}}\boldsymbol{F}_{\mathrm{c},i}^{\mathrm{p}}\right)+\boldsymbol{F}_{\mathrm{D}}+\boldsymbol{F}_{\mathrm{S}}+\boldsymbol{F}_{\mathrm{M}}+\boldsymbol{F}_{\mathrm{p}} \tag{5}$$

where m_{p} is the mass of particle p; ρ_{p} is the density of the particle; $\boldsymbol{F}_{\mathrm{c},i}^{\mathrm{p}}$ is the contact force acting on the first external spherical element of particle p (k_{c} is the number of spherical elements on the external surface of irregular particle); $\boldsymbol{F}_{\mathrm{D}}$ is the fluid drag force; $\boldsymbol{F}_{\mathrm{S}}$ is the shear lift or Saffman lift force; $\boldsymbol{F}_{\mathrm{M}}$ is the rotational lift or Magnus force; $\boldsymbol{F}_{\mathrm{p}}$ is the fluid pressure gradient force.

The rotational motion of particle p can be expressed as (Kuang et al., 2009):

$$\frac{\mathrm{d}}{\mathrm{d}t}\boldsymbol{I}_{\mathrm{p}}\boldsymbol{\omega}_{\mathrm{p}}=\sum_{e=1}^{k_{\mathrm{c}}}\left(\boldsymbol{T}_{\mathrm{t},e}^{\mathrm{p}}+\boldsymbol{T}_{\mathrm{r},e}^{\mathrm{p}}\right)+\boldsymbol{T}_{\mathrm{DT}}^{\mathrm{p}} \tag{6}$$

where the torque vectors of $\boldsymbol{T}_{\mathrm{t},e}^{\mathrm{p}}$ and $\boldsymbol{T}_{\mathrm{r},e}^{\mathrm{p}}$ ($e = 1,2 \ldots, k_{\mathrm{c}}$) are generated by tangential and normal contact forces acting on a particle of a specific element, the moment of inertia is $\boldsymbol{I}_{\mathrm{p}}$, the angular velocity of particle is $\boldsymbol{\omega}_{\mathrm{p}}$, and $\boldsymbol{T}_{\mathrm{DT}}^{\mathrm{p}}$ is the drag torque generated by rotation.

2.2.1. Contact force and torque

A schematic diagram of the collision forces between the elements of sub-circular particles is shown in Fig. 5. Combined with the study of Renzo and Maio (2004), the contact force of the element *j* of particle q on the element *i* of particle p is expressed as:

$$\boldsymbol{F}_{\mathrm{c},i}^{\mathrm{p}}=\boldsymbol{F}_{\mathrm{n},ij}+\boldsymbol{F}_{\mathrm{n},ij}^{\mathrm{d}}+\boldsymbol{F}_{\mathrm{t},ij}+\boldsymbol{F}_{\mathrm{t},ij}^{\mathrm{d}} \tag{7}$$

The normal contact force is:

$$\boldsymbol{F}_{\mathrm{n},ij}=\frac{4}{3}E^{*}\sqrt{R^{*}}\boldsymbol{\delta}_{\mathrm{n},ij}^{3/2} \tag{8}$$

where $\boldsymbol{\delta}_{\mathrm{n},ij}$ is the normal overlap of the particles; E^{*} is the equivalent Young's modulus; R^{*} is the equivalence radius; the normal damping force obtained is:

$$\boldsymbol{F}_{n,ij}^{\mathrm{d}}=-2\sqrt{\frac{5}{6}}\frac{\ln \mathrm{e}}{\sqrt{(\ln \mathrm{e})^{2}+\pi^{2}}}\sqrt{\boldsymbol{S}_{n,ij}m^{*}}\boldsymbol{v}_{\mathrm{n,pq}} \tag{9}$$

where m^{*} is the equivalent particle mass ($[1/m_i+1/m_j]^{-1}$), m_i and m_j are the contact masses of the element for i, j; $\boldsymbol{S}_{\mathrm{n},ij}=2E^{*}\sqrt{R^{*}\boldsymbol{\delta}_{\mathrm{n},ij}}$ is the normal stiffness; $\boldsymbol{v}_{\mathrm{n,pq}}$ is the normal velocity component at the contact point; e is the recovery coefficient. The normal contact force is:

$$\boldsymbol{F}_{\mathrm{t},ij}=\begin{cases}\mu_{\mathrm{s}}|\boldsymbol{F}_{\mathrm{n},ij}|\dfrac{\boldsymbol{v}_{\mathrm{t,pq}}}{|\boldsymbol{v}_{\mathrm{t,pq}}|} & |\boldsymbol{F}_{\mathrm{t},ij}|>\mu_{\mathrm{s}}|\boldsymbol{F}_{\mathrm{n},ij}|\\ -\boldsymbol{\delta}_{\mathrm{t},ij}\boldsymbol{S}_{\mathrm{t},ij} & |\boldsymbol{F}_{\mathrm{t},ij}|<\mu_{\mathrm{s}}|\boldsymbol{F}_{\mathrm{n},ij}|\end{cases} \tag{10}$$

where, $\boldsymbol{S}_{\mathrm{t},ij}=8G^{*}\sqrt{R^{*}\boldsymbol{\delta}_{\mathrm{t},ij}}$ is the tangential stiffness; G^{*} is the equivalent shear modulus; $\boldsymbol{\delta}_{\mathrm{t},ij}$ is the tangential overlap; μ_{s} is the sliding friction coefficient; $\boldsymbol{v}_{\mathrm{t,pq}}$ is the relative tangential velocity at the contact point. The tangential damping force is given as:

$$\boldsymbol{F}_{\mathrm{t},ij}^{d}=-2\sqrt{\frac{5}{6}}\frac{\ln \mathrm{e}}{(\ln \mathrm{e})^{2}+\pi^{2}}\sqrt{\boldsymbol{S}_{\mathrm{t},ij}m^{*}}\boldsymbol{v}_{\mathrm{t,pq}} \tag{11}$$

The traction force on the particle is the resultant force exerted by the fluid. Specifically, the drag force on particle p is:

$$\boldsymbol{F}_{\mathrm{D}}=0.5\rho_{\mathrm{f}}A_{\mathrm{p}}C_{\mathrm{D}}\left|\boldsymbol{u}_{\mathrm{f}}-\boldsymbol{u}_{\mathrm{p}}\right|\left(\boldsymbol{u}_{\mathrm{f}}-\boldsymbol{u}_{\mathrm{p}}\right)\varepsilon \tag{12}$$

where $\boldsymbol{u}_{\mathrm{f}}-\boldsymbol{u}_{\mathrm{p}}$ is the slip velocity; A_{P} is the frontal area of the particle; C_{D} is the coefficient of drag; ε is a function used to characterize the effect of the presence of other particles in the surrounding area.

Consequently, the drag torque generated acting on the particle p due to the fluid velocity is (Zhao et al., 2023):

$$\boldsymbol{T}_{\mathrm{DT}}^{\mathrm{p}}=\frac{\rho_{\mathrm{p}}}{2}\left(\frac{d_{\mathrm{p}}}{2}\right)^{5}C_{\mathrm{DR}}|\boldsymbol{\Omega}|\boldsymbol{\Omega} \tag{13}$$

where Re_{r} is the Reynolds number. C_{DR} is the rotational drag coefficient and $\boldsymbol{\Omega}$ is the angular velocity of the particle with respect to the fluid ($\boldsymbol{\Omega}=\nabla\times\boldsymbol{u}_{\mathrm{f}}/2-\boldsymbol{\omega}_{\mathrm{p}}$).

$$C_{\mathrm{DR}}=\begin{cases}\dfrac{12.9}{Re_{\mathrm{r}}^{0.5}}+\dfrac{128.4}{Re_{\mathrm{r}}}, 32\le Re_{\mathrm{r}}<1000\\ \dfrac{64\pi}{Re_{\mathrm{r}}}, Re_{\mathrm{r}}<32\end{cases} \tag{14}$$

2.2.2. Lifting force

The Saffman lift ($\boldsymbol{F}_{\mathrm{S}}$) and Magnus lift ($\boldsymbol{F}_{\mathrm{M}}$) are perpendicular to the direction of the relative velocity between the particle and the fluid (Saffman, 1968).

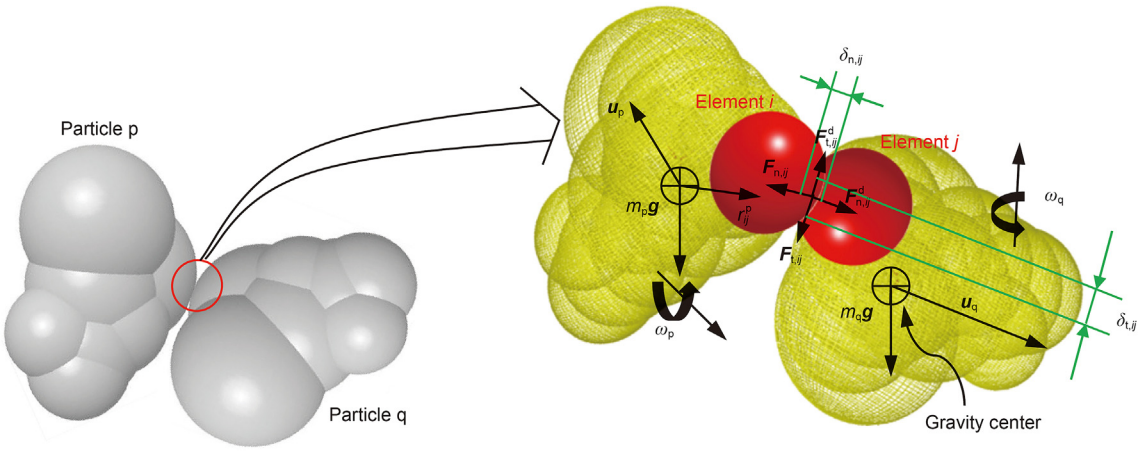

Fig. 5. Forces between contact units during the collision of particle p and particle q.

$$\boldsymbol{F}_{\mathrm{S}} = C_{\mathrm{LS}} \frac{\rho_{\mathrm{f}} \pi}{8} d_{\mathrm{p}}^{3} \left[\left(\boldsymbol{u}_{\mathrm{f}} - \boldsymbol{u}_{\mathrm{p}} \right) \times \boldsymbol{\omega}_{\mathrm{f}} \right] \tag{15}$$

where $\boldsymbol{\omega}_{\mathrm{f}}$ is the rotational velocity of the fluid, and C_{LS} is the coefficient of lift.

$$\boldsymbol{F}_{\mathrm{M}} = \frac{1}{8} \pi d_{\mathrm{p}}^{3} \rho_{\mathrm{f}} \boldsymbol{\omega}_{\mathrm{p}} \left(\boldsymbol{u}_{\mathrm{f}} - \boldsymbol{u}_{\mathrm{p}} \right) \tag{16}$$

The pressure gradient force ($\boldsymbol{F}_{\mathrm{p}}$), caused by fluid pressure differences across the surface of particle, is generally greater than the lift force (Ma et al., 2024).

$$\boldsymbol{F}_{\mathrm{p}} = -\frac{1}{6} \pi d_{\mathrm{p}}^{3} \frac{\mathrm{d}p}{\mathrm{d}x} \tag{17}$$

where d_{p} is the diameter of the particle, and $\frac{\mathrm{d}p}{\mathrm{d}x}$ is the pressure gradient along the x direction.

3. Modeling of intersected rough fractures

3.1. Morphology of rough fractures with different BI after fracturing

To ensure the reliability of the model, thin-section analysis and physical experiments for fracture propagation were combined with cores from the WC Formation in the LF block of the Pearl River Estuary Basin, China. The experimental parameters are shown in Table 2.

Combining rock sample #2 (BI_0.5) after fracturing depicted in Fig. 6(a) with the pumping pressure curve, it is evident that a vertically penetrating fracture formed, oriented perpendicular to the minimum horizontal principal stress direction (length: 500 mm, width: approximately 100 mm). Additionally, the fracture width of the hydraulic fracture is determined through inversion using the operational parameters. As illustrated in Fig. 6(b), the curve can be divided into three segments. The initial stage (0~t_1) is characterized by pressure accumulation. Upon activating the servo pump pressure system and gradually injecting the fracturing fluid, the pumping pressure in the sample increased linearly, reaching a rupture pressure of 18.9 MPa after t_1, resulting in fracture initiation. The subsequent stage (t_1~t_2) represents the main fracture formation phase, during which the creation of the primary fracture enlarges the internal space within the rock mass, leading to an instantaneous pressure drop. The final stage (t_2~t_3) signifies the extension of the main fracture, displaying a smooth curve with a typical symmetrical bimodal expansion pattern, and the fracture plane exhibits distinct rough surface features.

Owing to the strong heterogeneity of offshore tight sandstone, incorporating the brittleness index (BI) offers a comprehensive assessment of the elastic modulus and Poisson's ratio for characterizing reservoir properties. Fig. 7 illustrates the post-fracturing morphology of #1 (BI_0.4) and #3 (BI_0.62) under identical stress boundary conditions. Laboratory experiments revealed that a higher brittleness index in offshore rocks led to the formation of intricate and rough artificial fracture patterns.

Fig. 8(a) reveals that rock #4 (BI_0.55) with natural fractures is mainly composed of quartz sand. In addition, the fracturing result of the WC formation reflects a primary fracture (main fracture) perpendicular to the direction of the minimum horizontal principal stress. A transverse fracture (branch fracture) initiated in the middle, which occurred at 90° during propagation. The final morphology of the fracture manifests as an intersected shape (Fig. 8(b)). Due to the existence of natural fractures, the pumping pressure curve clearly exhibits a sawtooth shape.

3.2. Quantification of the roughness of the different fractures

3.2.1. Joint roughness coefficient and fractal dimension (D)

Natural rock is a complex geological body containing a large number of structural surfaces, the creation of which relies on the deformation, strength, and permeability characteristics of the rock, causing it to exhibit varying degrees of roughness (Filippov et al.,

Table 2
Experimental parameters of fracture propagation.

Parameters	Value	Parameters	Value
Primary fracture size, mm	500 × 100 × 2	Branched fracture size, mm	400 × 100 × 1
Fracturing fluid viscosity, Pa·s	0.005	Inlet opening	Full open
Fracturing fluid density, kg/m^3	1000	Fracture node morphology	Vertical
Injection rate, m/s	0.2	Fracture node location	1/2 of primary fracture

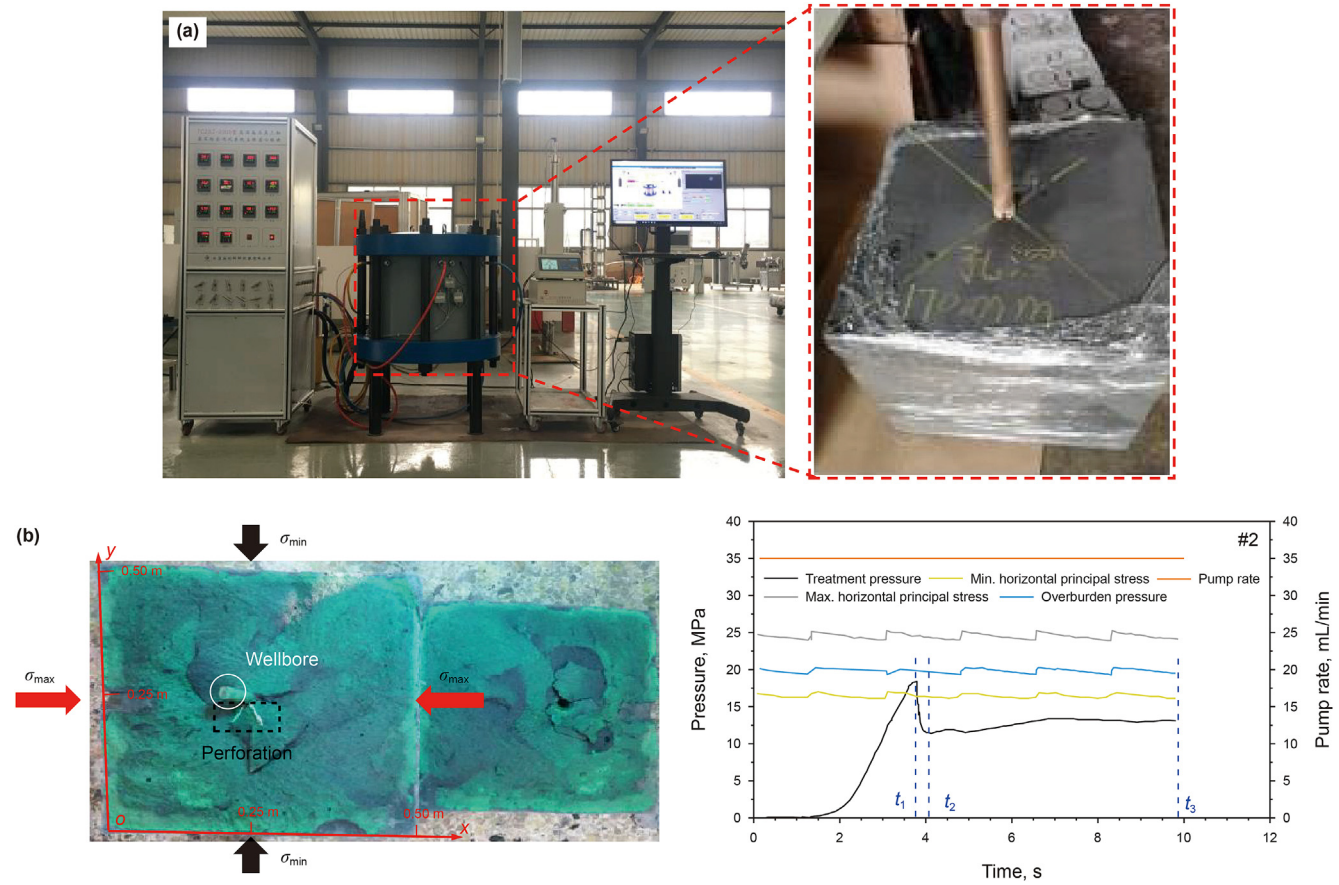

Fig. 6. (**a**) Test system. (**b**) Propagation of rock sample after fracturing and pump-pressure curve.

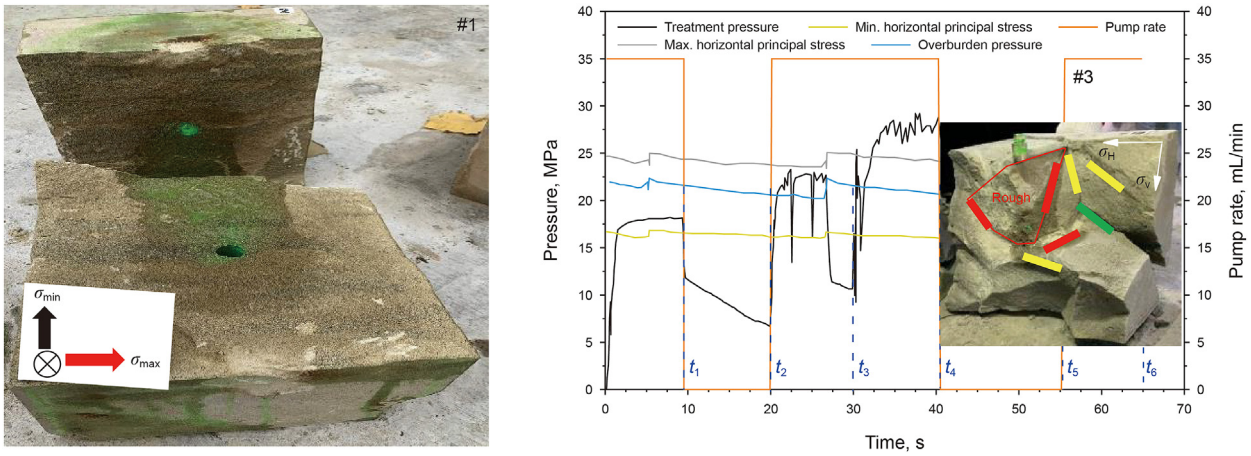

Fig. 7. Surfaces of fractures after fracturing of two different brittle rock samples.

2022; Martyushev et al., 2022). The American mathematicians Mandelbrot and Benoit (1983) proposed the theory of fractal geometry, which initiated the study of applications in various industries incorporating fractal geometry. Taking the fractured section of a rock as an example, one of the main characteristics of this object is its extreme irregularity. Thus, the most representative box dimension method in fractal calculations is applied in our research, which is commonly incorporated in mathematical calculations and empirical estimation of rock mechanics. The scale and the number of boxes in the fracture model of the scanned spatial coordinate system are calculated by the Cubic Covering Method (CCM) based on the theory of box dimensions. The scatter diagram of $\ln(1/\delta_i)$, $\ln N_{\delta_i}$ was plotted via least squares in a double logarithmic coordinate system (δ_i is the scale of calculation for the CCM; N_{δ_i} is the number of boxes) to obtain a linear regression line, which estimates the fractal dimension (D) of the measured rough fracture. Fractal dimension has been demonstrated to be larger for a constant scale, indicating a rougher rock surface.

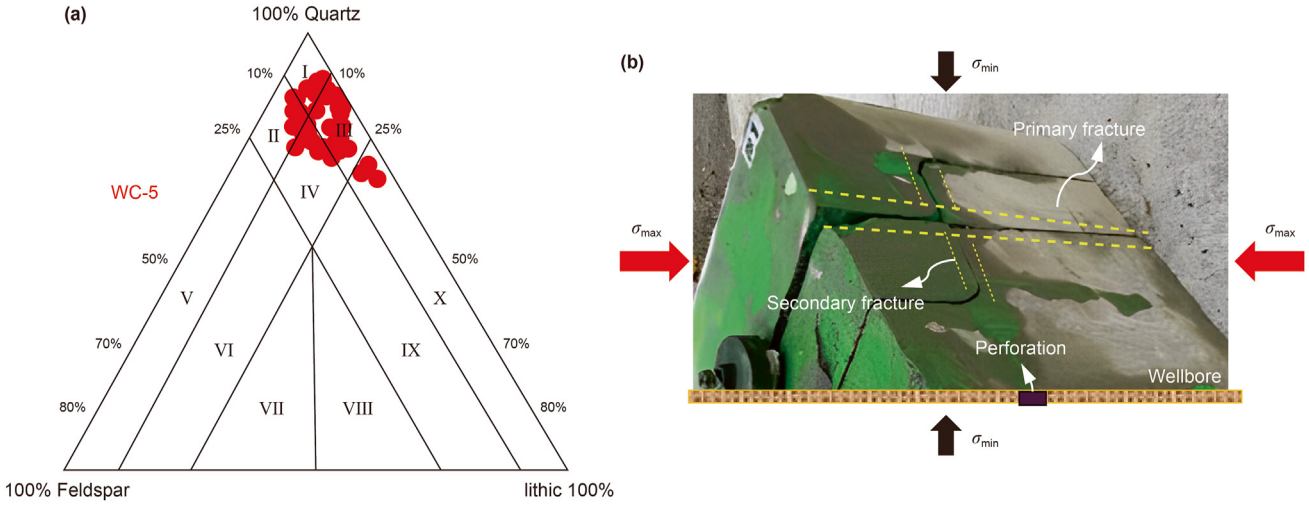

Fig. 8. (**a**) Rock composition. (**b**) Shape of intersected fractures after compression.

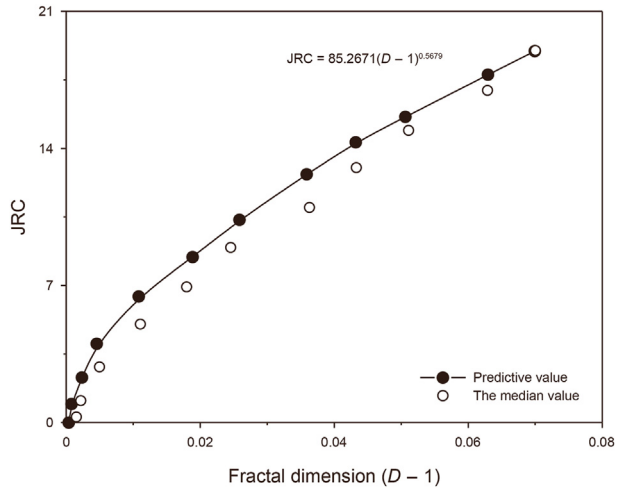

Fig. 9. Scatter diagram of typical contour lines and predicted values of the JRC.

Zhou and Xie (2003) established an empirical relationship between JRC and D through research on the fractal model. Using the median JRC values of the 10 contour lines as references, the fractal approximation method was applied to analyze these lines to obtain corresponding JRC (as shown in Fig. 9 with a comparison error of approximately 5%). This method is formulated to quantitatively describe the magnitude of the roughness of the rough surface. Accordingly, the JRC can quantitatively reflect the morphological characteristics of rough walls (Xie, 1995).

3.2.2. Quantitative identification process of roughness

Combined with the introduction, we conclude that the previous analytical models conducted in the study of the proppant transport process have certain limitations. The wall surface was smoothed, neglecting the impact of the rough surface on proppant transport; the study of a rough straight surface (only one fracture) ignored the influence of the presence of branch fractures. Extensive experiments confirmed the correlation between the BI of rock and the roughness of fractures post-hydraulic fracturing, a detail explicitly presented above. To characterize and establish the different rough fractures, we formulate the following quantitative process. ① Core scanning and Matlab were used to generate point cloud data for rough fracture modeling. Additionally, to reduce the amount of data and keep the surface smooth based on the actual fracture shape, fractal interpolation is applied to process the point cloud data to simulate the actual rough shape of the fracture (Dai and Liu, 2023). A Gaussian auto-correlation function is transformed for the rough surface dimensions as follows.

$$C_h(u,v) = \sigma_h{}^2 \exp\left[-\left(\frac{u}{l_{c1}}\right)^2 - \left(\frac{v}{l_{c2}}\right)^2\right] \tag{18}$$

where $C_h(u,v)$ is the auto-correlation function; $\sigma_h{}^2$ is the square of the overall roughness; u and v are the lags in x and y directions, respectively; l_{c1} and l_{c2} are the correlation length coefficients in the x, y directions. ② The histogram of the distribution of the frequency for aperture in the point cloud data is shown in Fig. 10(a), which reveals the apertures satisfy a Gaussian normal distribution. A combination of height and texture feature parameters is used to characterize the macroscopic undulation quantitatively. Eventually, the auto-correlation 3D surface is established after mapping the point cloud data into the Cartesian coordinate system (x,y,z) as Fig. 10(b). Where x and y correspond to the plane coordinates of each pixel point of the image and z corresponds to the RGB value of each pixel point. The quantification of roughness is an exceptionally complicated process. After binarizing the autocorrelated surface of 2D, a suitable threshold is applied. Subsequently, the grayscale image is thresholded using commercially available software for segmentation according to grayscale levels. In this work, a threshold value of 0 is set to implement the z coordinate.

③ Taking the grey-scale processed point cloud data in Fig. 10(b) as an example, the box dimension growth in the fractal dimension method is set to constants (100, 200, 350) to calculate the fractal dimension (D) after processing the point cloud data. The fitting results in Fig. 11 clearly reveal that the prediction fits better when boxwidth_incr is 200. Consequently, D is 1.17 according to the calculated slope, which is brought into the equation in Fig. 9 to obtain the joint roughness coefficient (JRC) of 31 for the fracture.

3.3. Establishment of rough fractures with different roughnesses (JRC)

Due to the limited number and large size of cores, four scans were performed on the same fracture surface. By processing the point cloud data and calculating the fractal dimension, the JRC

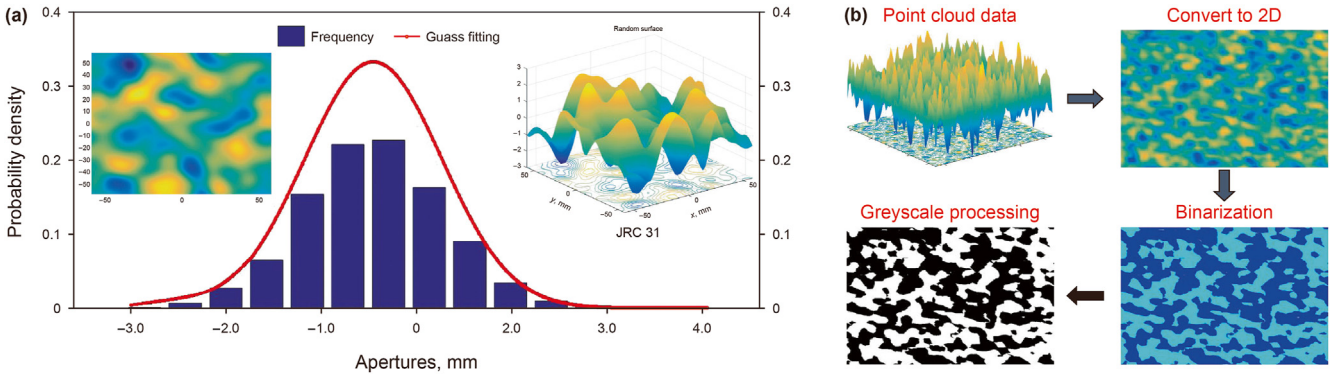

Fig. 10. (**a**) Frequency of aperture distribution when JRC is 31. (**b**) Processing of point cloud data.

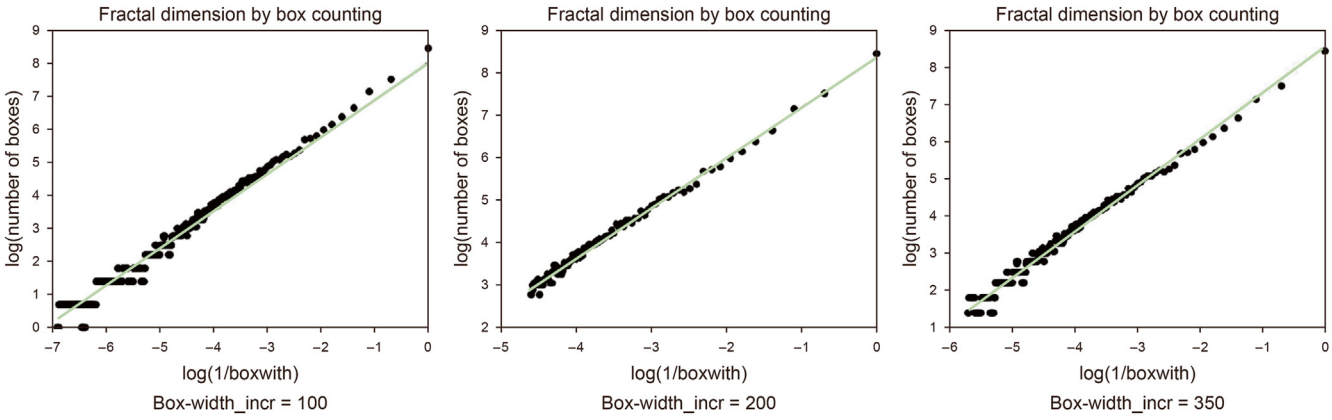

Fig. 11. Fitting plot of the box dimension with three different boxwidth_incr.

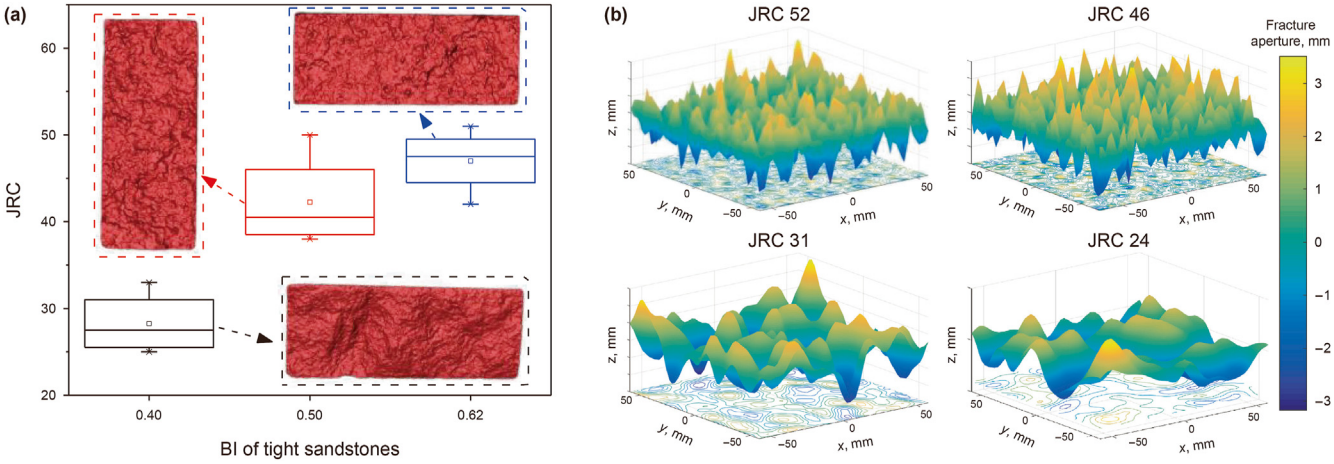

Fig. 12. (**a**) Distribution of JRC corresponding to different BIs after the experiment. (**b**) Point cloud data with different JRC created by Matlab.

distribution of fracture surfaces with three different BI was obtained as in Fig. 12(a), revealing a weak positive correlation between the BI of tight sandstone and JRC. However, the post-fracturing roughness of cores from the same reservoir is highly specific, limiting its representativeness for most rough fractures and its direct applicability for simulations. To address this, Matlab was used to generate autocorrelated point cloud data for fractures with arbitrary roughnesses. To explore the transport law of proppant in intersecting fractures under different roughnesses, fractures with JRC of 0, 24, 31, 46, and 52 were established according to the previous section, as shown in Fig. 12(b).

As aforementioned, to address the issue of low-order smoothness in transforming point cloud data into 3D surfaces, fractal interpolation calculations are conducted before establishing the rough surface. After the calculation of the fractal interpolation of the 3D surface, Fig. 13 indicates that the surface is smoothed well.

After comparison, intersecting fractures are verified to be more time-consuming to model and simulate than unilateral vertical

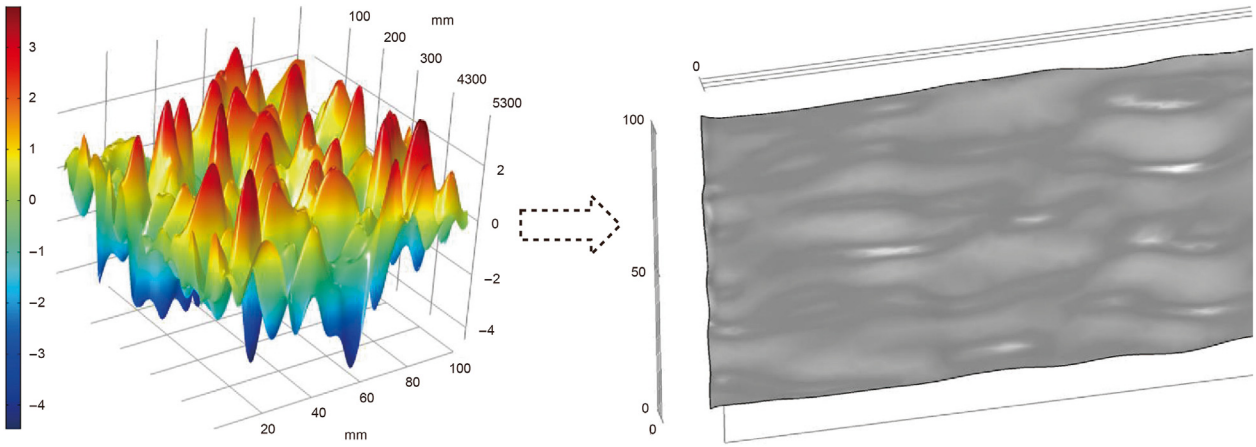

Fig. 13. Fractal interpolation function applied to smooth surfaces.

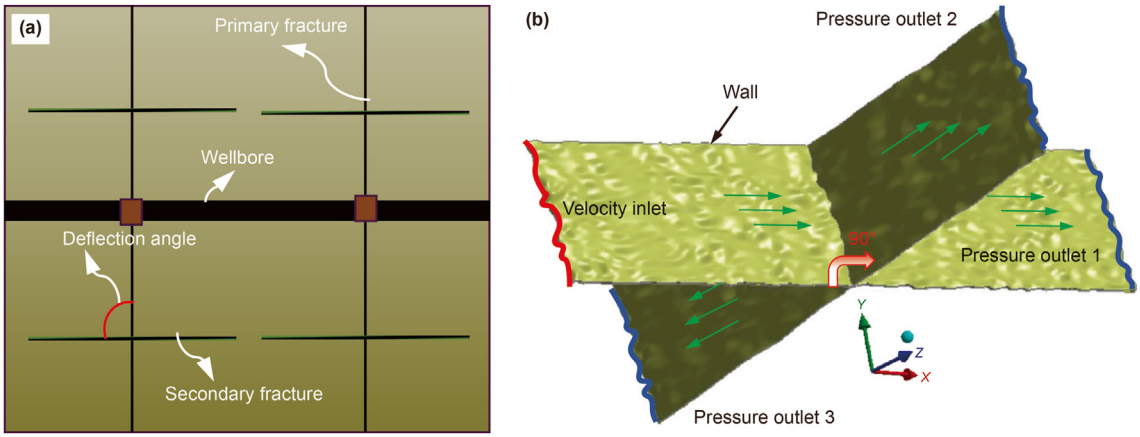

Fig. 14. (**a**) Schematic diagram of complex fractures at 90°. (**b**) 3D model of intersected rough fractures (JRC31).

fractures. However, the flow field for rough fractures performs relatively close to the actual conditions for proppant transport. Combining the result of fracture propagation in Fig. 8 and the imaging logging of the natural fracture distribution for representative wells, an intersecting coarse fracture of the same size was established with the parameters listed in Table 2. Fig. 14(a) illustrates a schematic model with a 90° angle between the main fracture and branch fracture. For computational convergence, the inlet boundary condition is specified as a velocity-inlet, three outlets are set as pressure-outlets, and the remaining boundaries are defined as walls. By incorporating Boolean operations, we established a complex rough model with JRC31, as shown in Fig. 14(b).

4. Validation of the computational model and analysis of the flow field

Since the literature on fracture experiments often involves analyzing fractures with bypass, we combined the distribution pattern from the experimental study by Tong and Mohanty (2017) on a smooth plate to verify the accuracy of the computational model (CFD-DEM). The basic parameters of the proppant injection experiment in the test and the subsequent simulation test parameters are listed in Table 3. As the simulation proceeds, comparing the morphology of the proppant bed in the simulation and the experiment (Fig. 15) reveals the shapes of the deposition derived from the experiment and the simulation presents fairly consistent results within reasonable errors. The negligible differences may be caused by the use of uncalibrated model parameters.

4.1. Mesh-independent verification

The parameters of the particles in the EDEM are consistent with the process of verification, where the initial JRC of the simulation is 31, and the branch fracture angle is 90°. The coupling time step is influenced by Young's modulus of the particles and increases as the minimum particle size decreases. For 0.6 mm particles, with Young's modulus of 1×10^{11} Pa and a Poisson's ratio of 0.2, the time step of DEM is set to 0.00015 s, which is 1/10 of the time step in CFD. The boundary conditions for analyzing the rough wall flow field are preset as follows: the velocity of inlet is 0.2 m/s; the outlet boundary condition is defined as a pressure outlet; the wall is defined as the nonslip wall. Moreover, the k-ε turbulence model of RNG is applied in the calculation. To ensure the accuracy of the calculation, the turbulence parameters at the inlet are defined in terms of the turbulence intensity and turbulence viscosity ratio for a specific value of 5%. In addition, the SIMPLEC algorithm was chosen to couple the velocity and pressure, whereas the discretization calculations for pressure, momentum, turbulence intensity and dissipation rate are in second-order windward format.

Given the complexity of the model, an unstructured tetrahedral mesh divides fluid computations. Ensuring mesh elements triple the proppant volume is pivotal for the bidirectional coupling

Table 3
Properties of the particles, fluids and overall model.

Parameters	Value of validate	Value of test	Unit
Main slot setup dimension	0.381 × 0.076	0.5 × 0.1 × 0.002	m
Bypass slot dimension	0.191 × 0.076	0.4 × 0.1 × 0.001	m
Fracture width	2	–	mm
Angle between two fractures	90	30, 45, 60, 90	degree
Inlet fluid velocity	0.1	0.3	m/s
Fluid viscosity	1	5	cp
Fluid density	998.2	998.2	kg/m^3
Particle diameter	0.595	0.6	mm
Particle load	0.84	0.84	lb/gal
Poisson's ratio	0.2	0.2	–
Young's modulus	1e^{11}	1e^{11}	Pa
Restitution coefficient	0.7	0.7	–
Static friction coefficient	0.5	0.5	–
Rolling friction coefficient	0.01	0.01	–
Morphology of particles	–	S1, S2, S3	–
JRC	Smooth	52, 46, 31, 24, Smooth	–

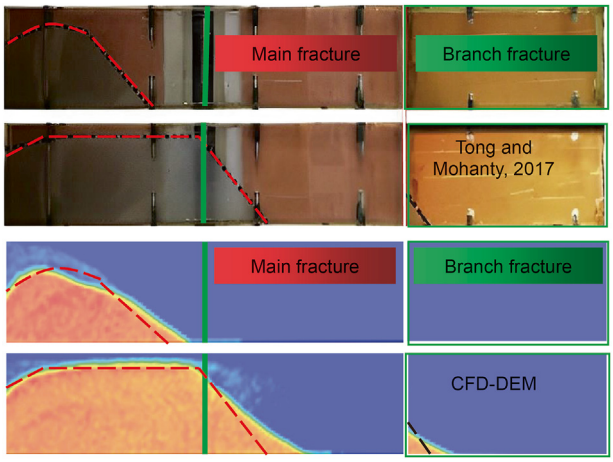

Fig. 15. Proppant bed profile for proppant injection into intersected fractures, validated by experiments with Tong and Mohanty (2017).

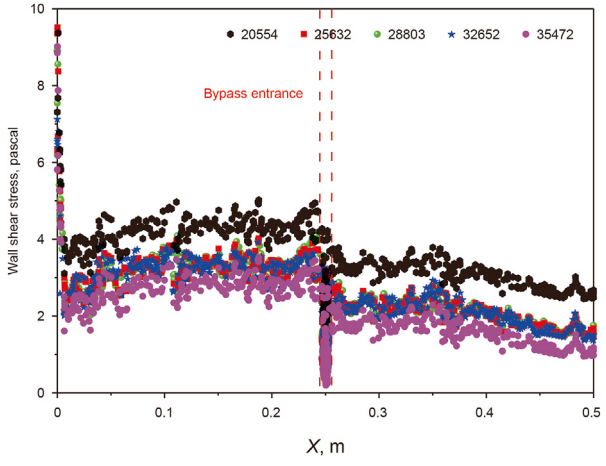

Fig. 16. Scatter diagram of wall shear at different x-coordinates on the cross-section.

model. To avoid sacrificing accuracy with excessively large elements, five meshes are introduced for mesh independence verification and precision. Wall shear gains significance in delineating flow on rough surfaces, controlling friction, and reflecting fluid obstruction due to the viscosity of the fracturing fluid (Deng et al., 2022). The simulation at the $z = 50$ mm cross section (Fig. 16) reveals a decrease in the wall shear stress from the inlet, which is notably reduced by branch fractures. Ultimately, the use of 25632 meshes ensures the accuracy of the model calculation while reducing the computation time.

4.2. Analysis of the flow field within rough intersecting fractures

To monitor the variation of the flow field after proppant deposition in the fracture under the same boundary conditions, we established five isometric planes (10, 30, 50, 70, and 90 mm) along the z-axis to output the contour of pressure (Fig. 17). The figure illustrates the pressure at the inlet (near the wellbore) decays gradually along each outlet, the conclusion of which is consistent with production.

Owing to the effect of the mean velocity gradient and buoyancy, the turbulent kinetic energy (k) determines the magnitude of the energy in the turbulent flow. More importantly, the effect of turbulence on the dissipation of particle energy in two-phase flow is not negligible and must be considered in the numerical analysis. Therefore, we monitor the turbulent kinetic energy of the cross section along the x-axis and the proppant deposition of each plane, as shown in Fig. 18.

Fig. 18 distinctly presents the relationship between the turbulent kinetic energy and particle deposition rate on each plane. Combined with the proppant deposition in EDEM (Fig. 19), the velocity of the proppant already deposited due to gravity tends to approach 0, and the proppant bed is basically kept motionless by the accumulation. This result can reasonably explain the conclusion

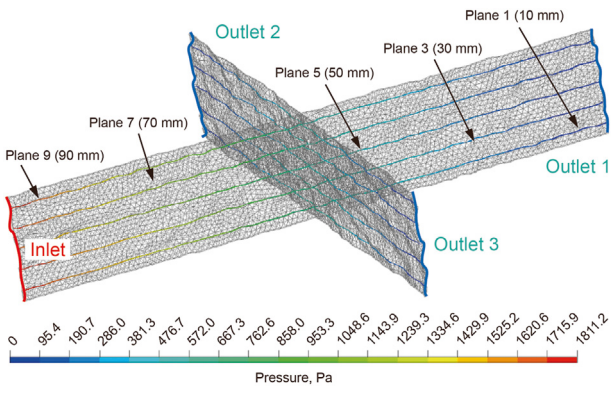

Fig. 17. Contour of the pressure distribution at different planes.

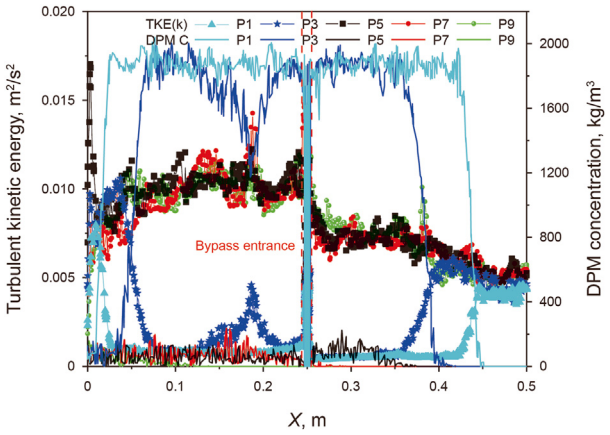

Fig. 18. Turbulent kinetic energy and particle deposition rate of different isometric planes in the main fracture along the *x*-axis direction.

that the turbulent motion of the proppant deposition is small while the concentration of discrete phase (DPM C) is large for each plane. The result, combined with the enlarged part at the intersection of fractures, clearly demonstrates a significant turbulence effect, leading to increased irregular movement of the proppant. Thus, this phenomenon increases the probability of particles colliding with the wall or particles when the proppant enters the branch fracture, resulting in a significant decrease in its velocity. Consequently, the velocities of particles on the left and right sides of the branch fracture are lower than the main fracture, and tree-like deposition is consistent with the rough fracture experiments carried out by Huang et al. (2019).

There are two main types of proppant transport within branch fractures: horizontal movement where the proppant is carried into the fracture under the action of fluid force. After the deposition reaches the equilibrium height, the proppant is carried to the back of the sand dike under the influence of fluidization in the upper part of the dike; under the action of gravity, the proppant settles in the fracture to form a sand mound. The colors on the particles in Fig. 20 represent the velocity of the proppant, while the colors on the fracture walls indicate the turbulent kinetic energy. Notably, regions with pronounced curvature on rough fractures exhibit higher turbulent kinetic energy on the wall. This phenomenon leads to the formation of plugging and gap effects, hindering the flow of subsequently injected proppant. Moreover, the enlarged portion of the figure shows closely spaced deposited particles. The wall exerts greater normal contact force on particles at locations where these effects occur, indicating that after fracture closure, proppants are more susceptible to embedment and crushing in areas with higher curvature, leading to reduced fracture conductivity.

To investigate the dynamic transport process of the proppant, the velocity and displacement of particle A (deposition in the main fracture) and particle B (deposition in the branch fracture) were tracked, respectively. The velocity-displacement-time curves of the monitored particles are shown in Fig. 21. Surprisingly, the proppant (particle A) has a longer time of suspended motion compared to particle B. Additionally, the collision between particles and the fracture walls causes particle B, initially moving along the *x*-axis in the branch fracture (red solid line on the coordinate axis), to shift and decelerate sharply along the *z*-direction, which is consistent with the results of the previous study. Accordingly, the transport distance of particle B, which entered the branch fracture after the collision, is only 0.35 m, shorter than the maximum distance of 0.45 m for the proppant that entered the main fracture.

5. Transport and deposition laws of the proppant

5.1. Effects of intersecting fractures with different roughnesses

The petrophysics of rocks largely depend on their constituents, which in turn significantly change the brittleness of rocks, causing tight sandstone, carbonate rock, and shale to exhibit different roughness sizes after fracturing. To systematically study the influence of different roughnesses on proppant transport, this study incorporates Matlab to construct point cloud data of different rock roughnesses. To better simulate the actual shape, the fractal interpolation method is applied to simulate the actual rough surface of the fracture, and five 90-degree fracture models with the same length and width and different roughnesses are established, as shown in Fig. 22.

Taking JRC46 as an example, the three selected moments of the transport process of the proppant and the contours of the turbulent kinetic energy on the wall are calculated (Fig. 23). As the proppant is continuously injected, the amount of proppant deposited at the bottom of the fracture will continuously increase due to gravity. Branch fractures amplify fluid turbulent kinetic energy near the wellbore, resulting in a gradual increase in the maximum turbulent kinetic energy with the growing proppant bed. At 18 s, it peaks at 3.8×10^{-2} m^2/s^2, which is 2.1 times greater than JRC31. This

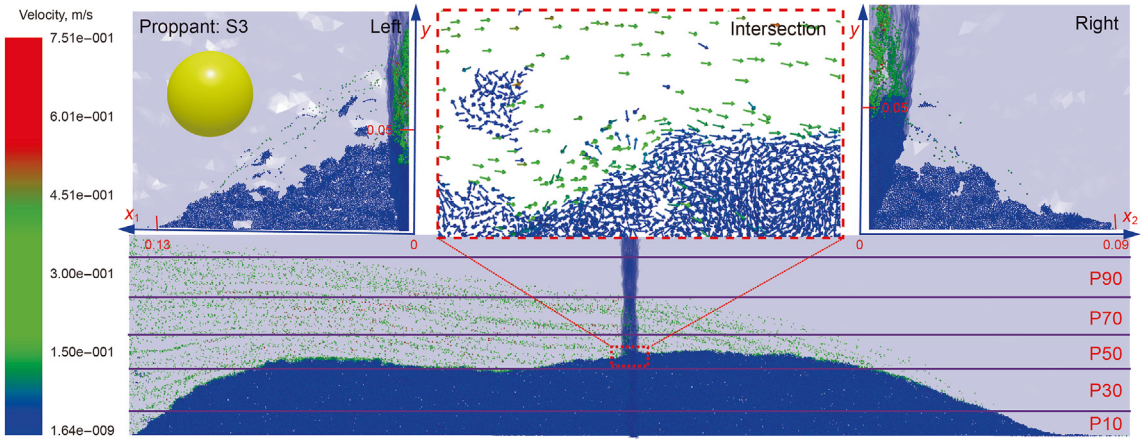

Fig. 19. Velocity distribution and deposition of proppant in fractures.

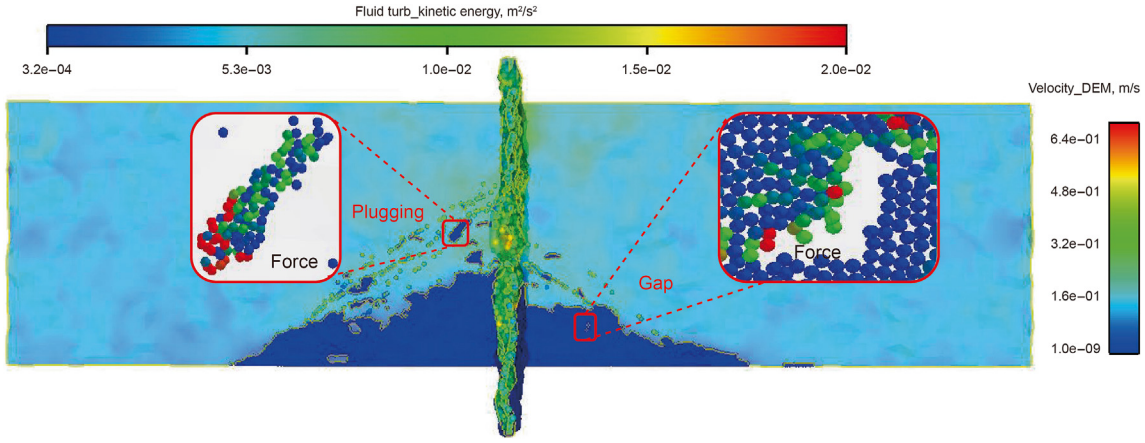

Fig. 20. Transport of proppant in the branch fracture.

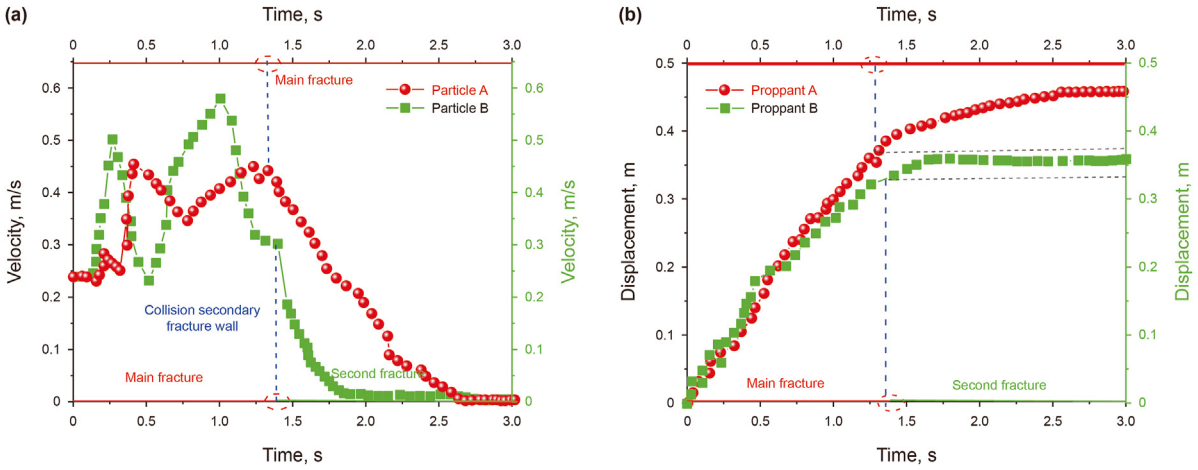

Fig. 21. Time-velocity-displacement curves of transport obtained through monitoring for two different proppants.

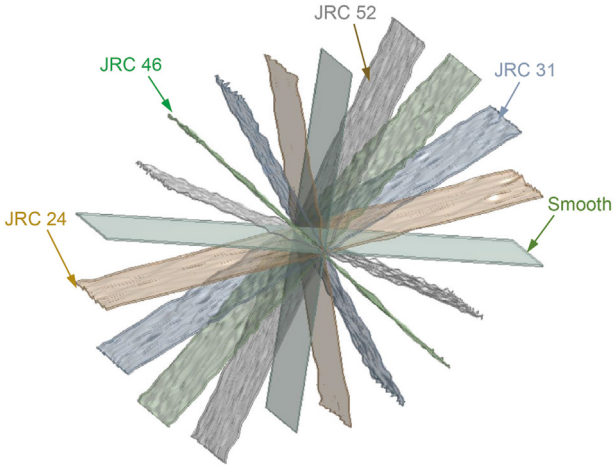

Fig. 22. Model of intersected fractures with different roughnesses.

phenomenon can carry post-injected particles to the back of the proppant bed, causing further proppant transport.

Combined with the fracture model established in Fig. 22, the results of the simulation test with the same parameters under the initial boundary conditions are shown in Fig. 24. Lines are added at the entrance of each proppant bed to visually represent the changes in the deposition angle. The results indicate that as roughness increases, both the deposition height of the proppant bed in the main fracture and the angle at the fracture entrance generally decrease. However, some of the differentiated patterns may result from localized proppant accumulation on rough fracture. Moreover, wall roughness delays the reduction in settling velocity and horizontal transport velocity of partial proppants as researched by Guo et al. (2022), thereby facilitating more proppants to form plugging or transport further, which is consistent with simulations. Proppant in intersecting fractures with large roughness accumulates at the bottom over longer distance, but the overall coverage area is not significantly different. Consequently, as the simulation time increases, more proppants deposit in the main fracture for rougher surfaces, while the proppant coverage in the narrower branch fractures is notably smaller.

The maximum proppant deposition height and coverage area in the branch fracture both occur at JRC31. This happens because the branch fracture is narrower than the main fracture, and excessive roughness causes proppant to clog at the intersection, hindering subsequent particle transport. Small roughnesses reduce the turbulent kinetic energy in the fracture, resulting in faster proppant deposition in the fracture. The comparison indicates that the deposition height and coverage area in the branch fracture of the smooth model decreased by 65.2% and 75.6%, respectively,

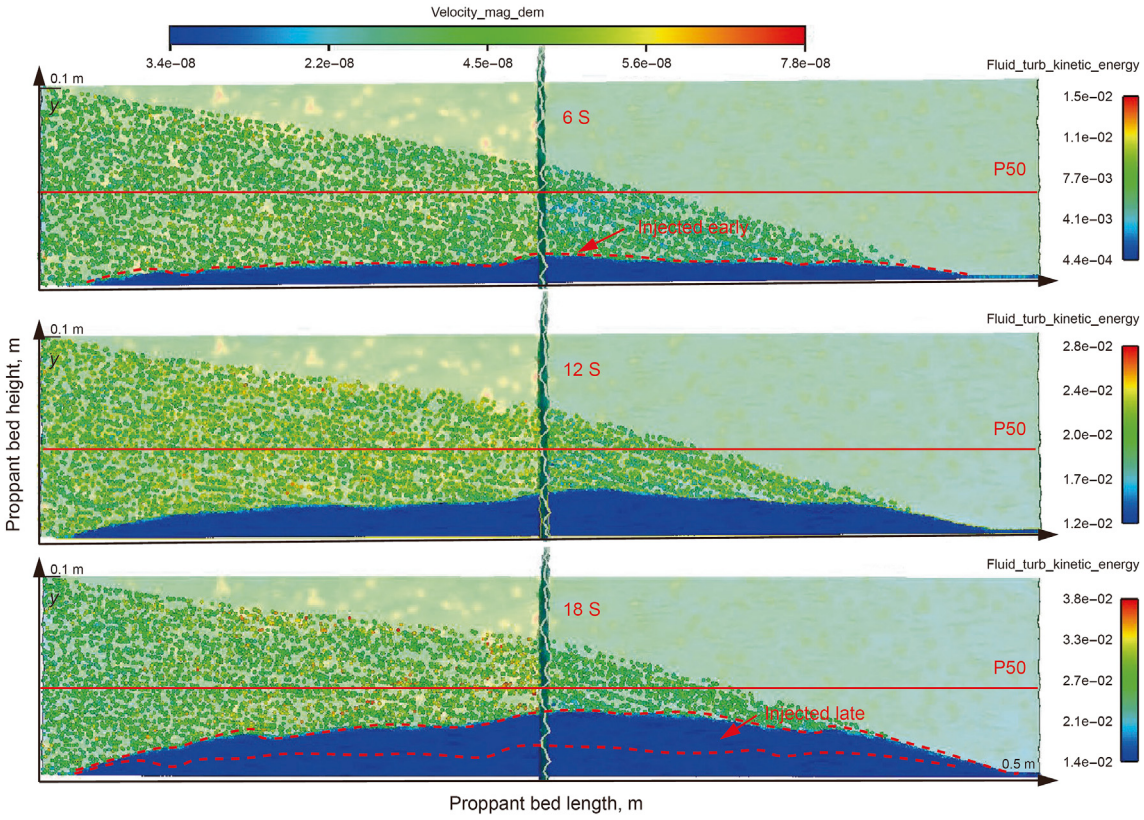

Fig. 23. Contours of the velocity and turbulent kinetic energy distributions of the proppant at different moments of JRC46.

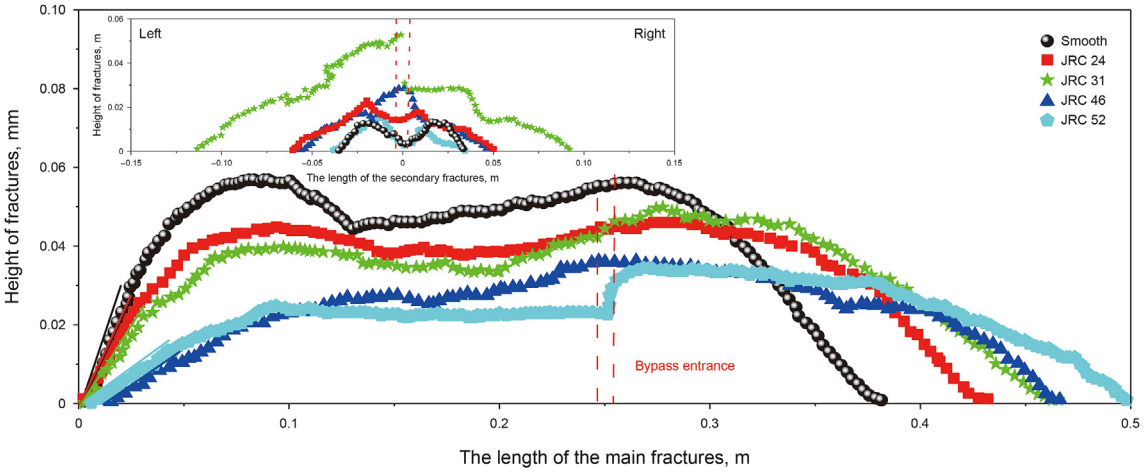

Fig. 24. Proppant deposition under different roughness of fracture.

compared to the intersected rough fracture model of JRC31 in Fig. 24. Therefore, targeting reservoirs with appropriate roughnesses for fracturing during production can significantly improve the effect of proppant placement.

5.2. Effects of different types of proppants

In the petroleum industry, sphericity is typically applied to describe the similarity between proppant and sphere (Xu et al., 2021). Due to the large difference in proppant shape between ceramic and quartz sand, larger ceramic particles with greater sphericity and quartz sand with relatively smaller sphericity are used in fracturing. To study the effects of different types of proppant, three typical proppant shapes are established under the premise of keeping a certain volume of proppant. These include sphere, sub-circular and rod-shaped proppants, as shown in Fig. 4, which are then imported into EDEM for coupling simulation.

The drag coefficient of nonspherical particles is determined by the Reynolds number, particle shape and direction of transport relative to the fluid. Fig. 25 illustrates the deposition of proppant (S1) in the intersecting fracture. For identical rough fracture, the S1 can form two distinct sand dikes in the main fracture compared with the spherical proppant (S3). The accumulation height, coverage area and distance of transport in the main fracture are

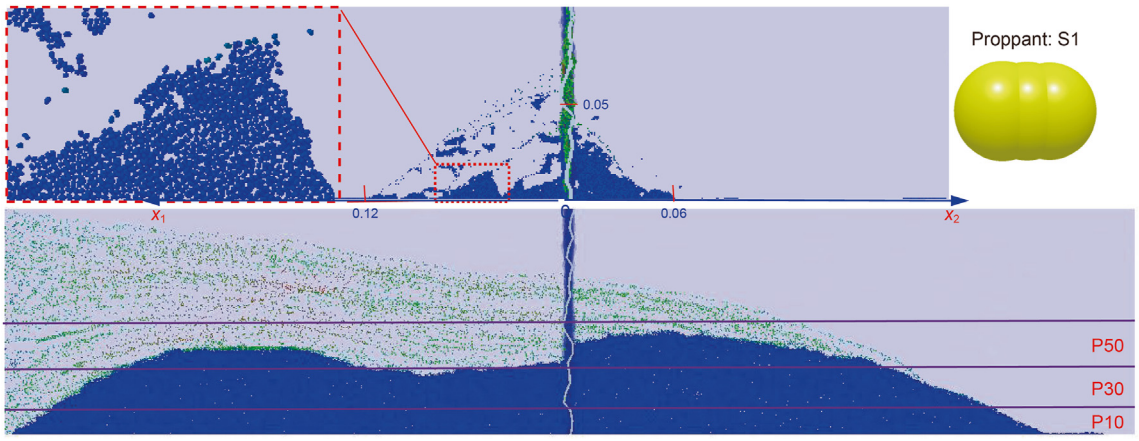

Fig. 25. Proppant deposition at sphericity of 0.92.

similar due to the small difference in sphericity, whereas the performance of the above indicators varies tremendously in the branch fracture for S1 and is significantly smaller than S3. Upon the enlarged portion, the noticeably smaller concentration of proppants deposit in the branch fracture is influenced by the shape of the proppant, thereby affecting the support effectiveness.

Fig. 26 shows the deposition of the quartz sand proppant (S2) with lower sphericity. A comparison of the proppants placement in Figs. 18 and 19 reveals the height of the proppant bed in the main fracture is much lower than that of S1 and S3 at 18 s. Additionally, proppant S2 is carried farther by the fracturing fluid, while the area of deposition is similar. The transport of the low-sphericity proppant (0.78) in the main fracture creates a fixed channel (red solid line), which causes a "jagged" effect at the top of the deposit. The distance and height of the proppant transported in the branch fractures are lower compared to S1 and S3. Due to the limited width of the branch fracture and the irregularity of the proppant, more effects of plugging and gap are formed in rough walls with high curvature. From the enlarged part on the left of Fig. 26, most of the proppant gathered near the intersection, greatly hindering the transport of proppant to the branched fracture (more significant velocity reduction for particles with small sphericity). Compared to the spherical proppant (S3), the proppant (S2) with smaller sphericity is sparsely distributed per unit area in the fracture. Consequently, in production, spherical particles are selected to ensure a longer distance of proppant transport in branch fractures, which is consistent with the actual fracturing process.

5.3. Different fracture intersection angles

During fracture production, the orientation of the fractures is influenced by a combination of factors such as the ground stress difference, production conditions and matrix conditions, which are characterized by the inclination angles between the main and branch fractures. Therefore, this approach is applicable to the study of the transport law of proppant in artificial and natural fractures. Since the model is shown along the *x*-*z* plane, four different intersection angles of 30°, 45°, 60° and 90° are set in this section, as shown in Fig. 27(a). *H* is used to describe the length of the branch fracture along the *z*-axis for the four intersected rough fractures.

Comparing Figs. 16 and 18, a significant similarity in the distribution of wall shear stress and turbulent kinetic energy within the flow field is observed, particularly at branch fractures. Focusing on the shear force distribution, Fig. 27(b) with scatter plots for four different angles distinctly shows a decrease in wall shear stress at the intersection as the angle approaches 90°. The maximum wall shear stress is 15.3 Pa when the angle is 30° for intersected fracture. The higher turbulent kinetic energy and wall shear lead to an increased probability of particle collision, which affects the effect of proppant transport. To analyze the influence of the fracture intersection angle on proppant transport more systematically, the deposition of proppant in Fig. 28 was obtained via coupled CFD-

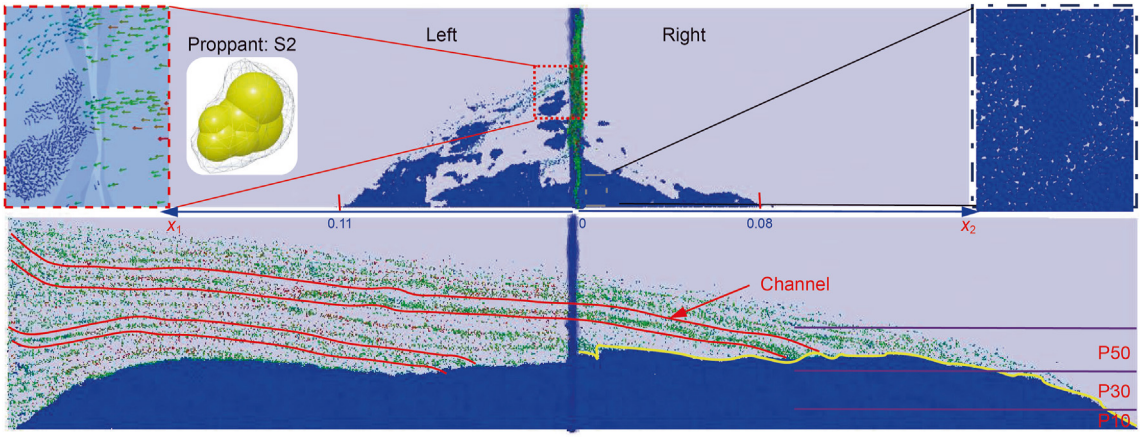

Fig. 26. Deposition of the quartz sand proppant (S2) with a sphericity of 0.78.

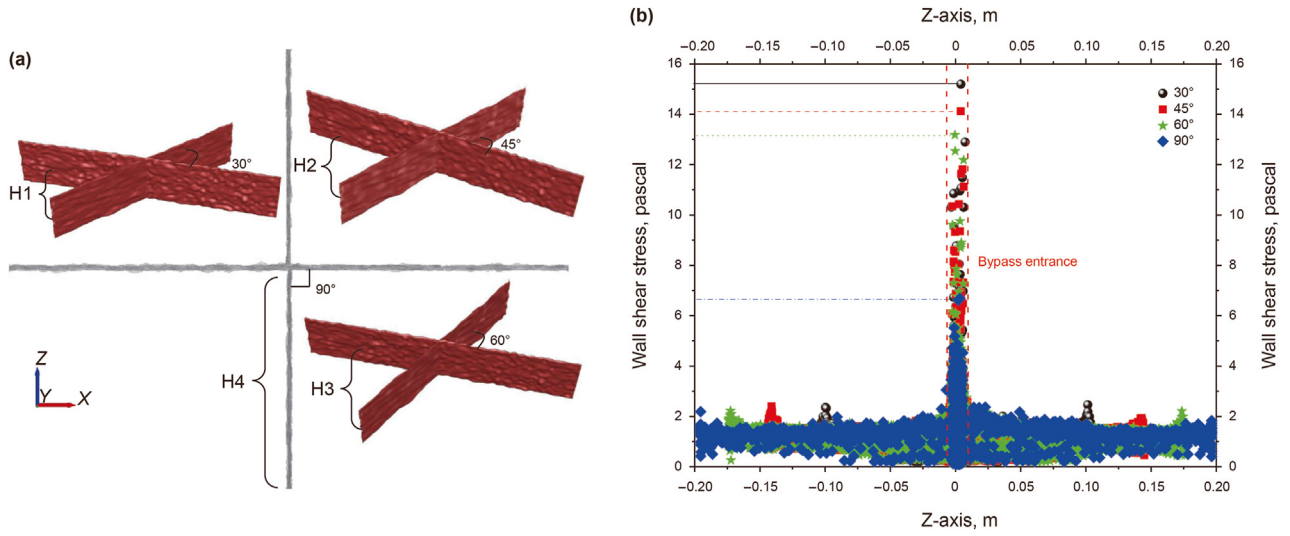

Fig. 27. (**a**) Schematic diagram of the intersected fracture distribution at four different angles. (**b**) Scatter diagram of the shear force along the *z*-axis for four different angles.

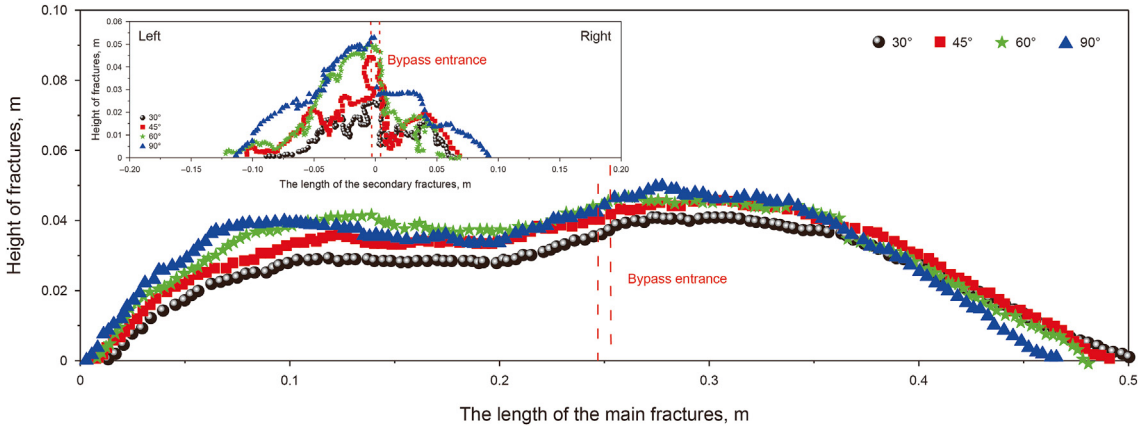

Fig. 28. Scatter diagram of proppant deposition under different fracture intersection angles.

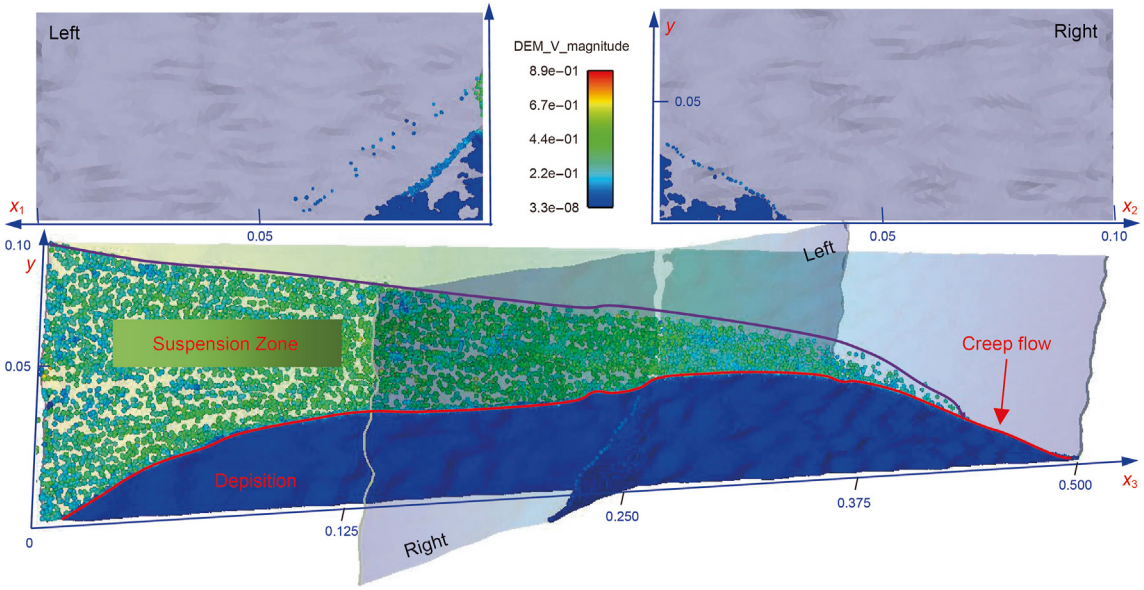

Fig. 29. Deposition of proppant in intersecting fracture (30°).

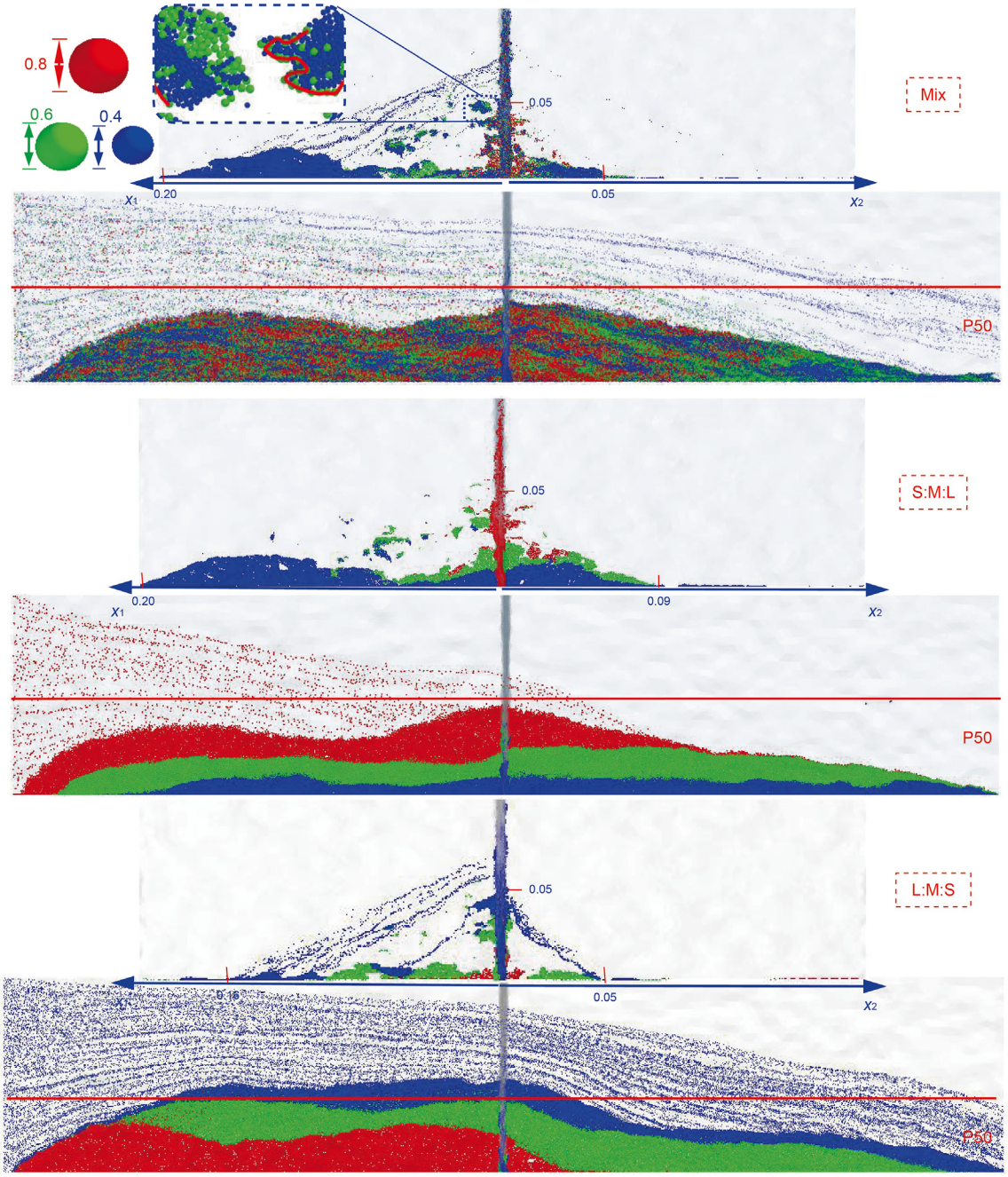

Fig. 30. Deposition of proppant under three different injection methods.

DEM simulation under the premise of the single variable. The figure obviously reveals the height of the proppant bed in the main fracture slightly increases with increasing angle, accompanied by a slight reduction in transport distance, while the area covered in the main fracture remains relatively unchanged. Surprisingly, an obvious difference was observed in the branch fracture. The monitoring results show that as the angle decreases, the turbulent kinetic energy and wall shear at the intersection increase, leading to an increased probability of proppant-wall collision, which reduces the placement height and area of the branching fractures and leads to more irregular bottom deposition.

For example, at a small angle of 30°, Fig. 29 shows two inconspicuous peaks occurring in the proppant bed deposited in the main fracture, with blue particles at the bottom where the particle velocity is 0 forming the deposition zone. The red part shows the particles creeping at the top, transporting the subsequently injected particles to transport farther. The area between the red and the brown solid line is the suspension zone, which gradually becomes covered as the proppant bed continues to rise. Compared with the deposition of branch fracture in Fig. 19, the small intersection angles cause the proppant to move mostly in the main fracture, whereas fewer proppants enter the branch fractures, resulting in inefficient transport.

5.4. Effects of different sequences of proppant injected

During the fracturing construction process, multistage pumping of different proppant sizes is often adopted to control the amount of

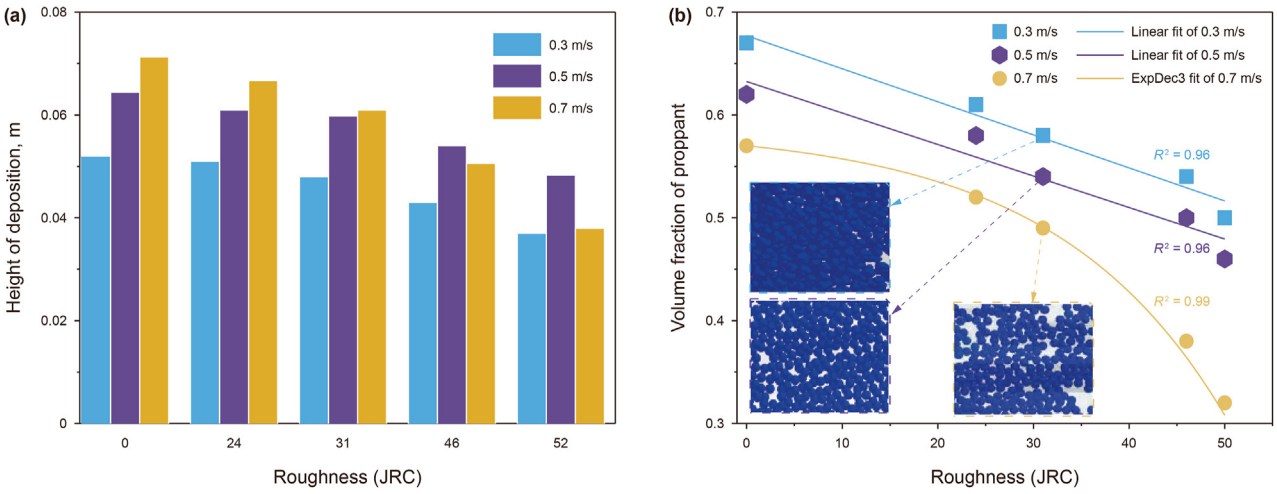

Fig. 31. (**a**) Height of deposition in branch fractures with different roughness-velocity. (**b**) Volume fraction of proppant with different roughness-velocity.

deposition near the entrance of the fractures to prevent the aperture from reclosing or blocking near-well fractures after the pump is stopped. Currently, few experimental studies exist on the effects of different size combinations of proppant injection sequences on the fracture filling effect. Based on the aforementioned experiments on smooth fracture, this section designs an experimental scheme for determining the filling effect of different proppant combinations (mixed particle size (Mix), small(S)-medium(M)-large(L) and (L)-(M)-(S)) according to the pumping habits at the fracturing site. The simulation of different proppant sizes on fracture is carried out to uncover the effect of the injected sequence on proppant deposition, which provides effective guidance for improving the rationality of pumping designed for fracturing.

Fig. 30 shows the proppant deposition of three different injection methods at the same moment. The comparison demonstrates that the injection method of S:M:L transports proppants over 80% of the distance achieved by the L:M:S within the branch fractures. In contrast, the initial injection sequence of large proppants results in a generally elevated proppant bed front, significantly reducing the sand-carrying capacity of the fracturing fluid. The sequence of L:M:S tends to cause blockage near the well and prevents the transport of post-injected proppant into the branch fracture. Moreover, larger proppants (0.8 mm) of mixed sizes can be transported farther along with smaller proppants, but effectiveness in entering rough branch fractures may be limited. Yet, larger curvature walls within the branch fracture tend to have plugging effects when obstructed by larger proppants (shown in enlarged Mix of Fig. 30). Consequently, when the fracture closes, smaller proppants near the well reduce the effective conductivity of the fracture, thus recommending the combination of S:M:L.

5.5. Effects of the synergistic influence of the injection rates and roughnesses

The analysis revealed that differences in proppant placement under varying degrees of roughness are primarily presented in branch fractures. To investigate the synergistic influences of velocity and roughness on proppant placement, a calculation time of 18 s was employed. As the velocity of the fracturing fluid reaches 0.7 m/s, some proppant flows out of the branch fractures. Consequently, the proppant concentration and bed height were monitored to evaluate placement effectiveness.

Fig. 31(a) shows that increasing the fracturing fluid flow rate raises the proppant deposition height in branch fractures. However, as the fracture roughness increases, the deposition height decreases. At JRC $\geq$ 46, greater velocity (0.7 m/s) causes local blockages, reducing the deposition height compared to 0.5 m/s. Fig. 31(b) indicates at higher flow rates, the proppant volume fraction per unit area decreases significantly. Eventually, with increasing roughness, the volume fraction decreases linearly at 0.3 and 0.5 m/s, but decreases exponentially at 0.7 m/s. Greater roughness of fractures during production requires a lower displacement of injection to ensure a greater spreading concentration of proppant.

By scanning the fracture surface after hydraulic fracturing, the approximate distribution of rock surface roughness (JRC) can be obtained for different blocks. Moreover, the daily production variation of a single well and the natural fracture distribution obtained from imaging logging were used to optimize the proppant size, fracturing fluid injection rate and proppant injection sequence to ensure the long-term stable flow conductivity of the fracture after fracture closure. Additionally, there is a strong correlation between lithology and post-fracturing roughness. Future studies with more field data can explore the relationships between various lithologies and optimal production parameters, providing systematic guidance for oilfield production.

6. Conclusion

The quantification of rough hydraulic fractures has been a challenging issue for scholars. The (Computational Fluid Dynamics) CFD-DEM (Discrete Element Method) model was verified to be highly accurate in simulating the proppant transport process by comparison with previous experimental results. Ultimately, the turbulent kinetic energy in the flow field is the primary factor affecting the process of proppant transport within rough fractures, which is not clearly evident in the deposition area. Some new findings were obtained as follows:

1. Owing to the strong heterogeneity of offshore reservoirs, experiments have revealed formations with higher brittleness index (BI) are positively correlated with the post-fracturing joint roughness coefficient (JRC), resulting in more complex and rougher fracture morphologies.
2. Fractures of JRC46 exhibit 2.1 times greater turbulent kinetic energy than JRC31, leading to more irregular motion of the proppants. Excessive roughness (JRC $\geq$ 46) hinders proppant transport into branch fractures, decreasing proppant bed height and coverage by 65.2% and 75.6%, respectively, compared with

JRC31. Conversely, smoother models reduce turbulent kinetic energy, causing faster proppant deposition and hindering subsequent injections.

3. Spherical proppants ensure optimal performance of placement in branch fractures. Additionally, decreasing sphericity results in a sparser density of deposition, leading to insufficient support during the subsequent closure of the fractures.
4. When the fracture angle increases from 30° to 90°, the maximum shear force at the intersection of fractures decreases to 40% at 30°. With increasing intersection angle, the proppant bed in the main fracture changes slightly, whereas the accumulation height and coverage area of the proppant bed in the branch fracture increase by more than 50%, respectively.
5. When the post-fracturing roughness of fractures in the target reservoir exceeds 46, proppants should be preferentially injected in a sequence from smaller to larger particles (S:M:L), and the velocity of fracturing fluid should be maintained at less than 0.7 m/s. Conversely, using a large-to-small sequence (L:M:S) may quickly cause blockage near perforations in offshore reservoirs with high BI, hindering subsequent proppant injection.
6. A systematic study of reservoir roughness patterns can optimize production parameters. With increasing fracture surface roughness, a greater velocity and smaller proppant sphericity lead to lower concentrations of proppant deposition on the rough surfaces. Specifically, at a velocity of 0.7 m/s, the deposition concentration shows an exponential decline.

CRediT authorship contribution statement

Biao Yin: Writing – original draft, Methodology, Conceptualization. **Yi-Shan Lou:** Validation, Supervision, Funding acquisition. **Shan-Yong Liu:** Investigation, Data curation. **Yan Zhang:** Validation, Supervision.

Availability of data and materials

Data will be made available on request.

Conflict of interests

The authors declare that there are no conflict of interests.

References

Akhshik, S., Rajabi, M., 2022. Simulation of proppant transport at intersection of hydraulic fracture and natural fracture of wellbores using CFD-DEM. Particuology 63, 112–124. https://doi.org/10.1016/j.partic.2021.05.005.

Alotaibi, M.A., Miskimins, J.L., 2015. Slickwater proppant transport in complex fractures: new experimental findings & scalable correlation. In: SPE Annual Technical Conference and Exhibition, Houston, Texas, USA. SPE-174828-MS. https://doi.org/10.2118/174828-MS.

Aminnia, N., Adhav, P., Darlik, F., et al., 2023. Three-dimensional CFD-DEM simulation of raceway transport phenomena in a blast furnace. Fuel 334, 126574. https://doi.org/10.1016/j.fuel.2022.126574.

Barton, N., 1973. Review of a new shear-strength criterion for rock joints. Eng. Geol. 7 (4), 287–332. https://doi.org/10.1016/0013-7952(73)90013-6.

Basiuk, L., Roschzttardtz, F.I., Fernández, M.E., et al., 2021. Proppant transport in scaled experiments: effect of drainage configuration and fracture wall roughness. J. Petrol. Sci. Eng. 208, 109433. https://doi.org/10.1016/j.petrol.2021.109433.

Dai, Z., Liu, S., 2023. Construction and box dimension of the composite fractal interpolation function. Chaos, Solit. Fractals 169, 113255. https://doi.org/10.1016/j.chaos.2023.113255.

Deng, F., Yin, B., Li, X., Wang, Y., Xu, Y., 2022. Analysis of the scaling mechanism and characteristics of a double-defects screen based on data from Hafaya Oilfield. J. Petrol. Sci. Eng. 216, 110729. https://doi.org/10.1016/j.petrol.2022.110729.

Dontsov, E.V., Peirce, A.P., 2014. Slurry flow, gravitational settling and a proppant transport model for hydraulic fractures. J. Fluid Mech. 760, 567–590. https://doi.org/10.1017/jfm.2014.606.

Filippov, E.V., Zaharov, L.A., Martyushev, D.A., 2022. Reproduction of reservoir pressure by machine learning methods and study of its influence on the cracks formation process in hydraulic fracturing. J. Mining Inst. 258, 924–932. https://doi.org/10.31897/PMI.2022.103.

Guo, T.K., Luo, Z.L., Zhou, J., et al., 2022. Numerical simulation on proppant migration and placement within the rough and complex fractures. Petrol. Sci. 19 (5), 2268–2283. https://doi.org/10.1016/j.petsci.2022.04.010.

Huang, H., Babadagli, T., Li, H.A., et al., 2019. Effect of injection parameters on proppant transport in rough vertical fractures: an experimental analysis on visual models. J. Petrol. Sci. Eng. 180, 380–395. https://doi.org/10.1016/j.petrol.2019.05.009.

Kern, L.R., Perkins, T.K., Wyant, R.E., 1959. The mechanics of sand movement in fracturing. J. Petrol. Technol. 11 (7), 55–57. https://doi.org/10.2118/1108-G.

Kruggel-Emden, H., Rickelt, S., Wirtz, S., Scherer, V., 2008. A study on the validity of the multi-sphere discrete element method. Powder Technol. 188 (2), 153–165. https://doi.org/10.1016/j.powtec.2008.04.037.

Kuang, S.B., Yu, A.B., Zou, Z.S., 2009. Computational study of flow regimes in vertical pneumatic conveying. Ind. Eng. Chem. Res. 48 (14), 6846–6858. https://doi.org/10.1021/ie900230s.

Liu, B., Yao, J., Sun, H., Zhang, L., 2024. Effects of natural fracture reopening on proppant transport in supercritical. Geoenergy Sci. Eng. 238, 212906. https://doi.org/10.1016/j.geoen.2024.212906.

Ma, H., Li, B., Zhang, S., 2024. Scour mechanism around a pipeline under different current-wave conditions using the CFD-DEM coupling model. Comput. Geotech. 170, 106304. https://doi.org/10.1016/j.compgeo.2024.106304.

Martyushev, D.A., Yang, Y., Kazemzadeh, Y., et al., 2023a. Understanding the mechanism of hydraulic fracturing in naturally fractured carbonate reservoirs: microseismic monitoring and well testing. Arabian J. Sci. Eng. 49 (6), 8573–8586. https://doi.org/10.1007/s13369-023-08513-1.

Martyushev, D.A., Ponomareva, I.N., Filippov, E.V., 2023b. Studying the direction of hydraulic fracture in carbonate reservoirs: using machine learning to determine reservoir pressure. Petroleum Res. 8 (2), 226–233. https://doi.org/10.1016/j.ptlrs.2022.06.003.

Martyushev, D.A., Ponomareva, I.N., Filippov, E.V., 2022. Formation of hydraulic fracturing cracks in complicated carbonate reservoirs with natural fracturing. Bullet. Tomsk Polytechnic Univ. Geo Assets Eng. 333 (1), 85–94. https://doi.org/10.18799/24131830/2022/1/3212.

Mandelbrot, Benoit, B., 1983. The fractal geometry of nature. Am. J. Phys. 51, 286–287. https://doi.org/10.1119/1.13295.

Opoku, F., Uddin, M.N., Atkinson, M., 2023. A review of computational methods for studying oscillating water columns—the Navier-Stokes based equation approach. Renew. Sustain. Energy Rev. 174, 113124. https://doi.org/10.1016/j.rser.2022.113124.

Patankar, N.A., Joseph, D.D., Wang, J., et al., 2002. Power law correlations for sediment transport in pressure driven channel flows. Int. J. Multiphas. Flow 28 (8), 1269–1292.

Qu, H., Liu, Y., Lin, H., et al., 2021. 3D CFD-DEM simulation and experiment on proppant particle-fluid flow in a vertical, nonplanar fracture with bends. Int. J. Multiphas. Flow 146, 103873. https://doi.org/10.1016/j.ijmultiphaseflow.2021.103873.

Qu, H., Xu, Y., Hong, J., et al., 2023a. Experimental and visual analysis of proppant-slickwater flow in a large-scaled rough fracture. SPE J. 28 (2), 477–495. https://doi.org/10.2118/212283-PA.

Qu, H., Xu, Y., Liu, Y., et al., 2023b. Experimental study of fluid-particle flow characteristics in a rough fracture. Energy 285. https://doi.org/10.1016/j.energy.2023.129380.

Renzo, A.D., Maio, F., 2004. Comparison of contact-force models for the simulation of collisions in DEM-based granular flow codes. Chem. Eng. Sci. 59 (3), 525–541. https://doi.org/10.1016/j.ces.2003.09.037.

Saffman, P.G., 1968. The lift on a small sphere in a slow shear flow-corrigendum. J. Fluid Mech. 31 (3), 624. https://doi.org/10.1017/S0022112068999990.

Sahai, R., Miskimins, J.L., Olson, K.E., 2014. Laboratory results of proppant transport in complex fracture systems. In: SPE Hydraulic Fracturing Technology Conference and Exhibition. February, Texas, USA. https://doi.org/10.2118/168579-MS. SPE-168579-MS.

Sievert, J.A., Wahl, H.A., Clark, P.E., et al., 1981. Prop transport in a large vertical model. In: SPE Rocky Mountain Petroleum Technology Conference/Low-Permeability Reservoirs Symposium. Denver, Colorado. SPE-9865-MS. https://doi.org/10.2118/9865-MS.

Suri, Y., Islam, S.Z., Hossain, M., 2020. Effect of fracture roughness on the hydrodynamics of proppant transport in hydraulic fractures. J. Nat. Gas Sci. Eng. 80, 103401. https://doi.org/10.1016/j.jngse.2020.103401.

Tang, P., Li, H., Zeng, J., 2022. Numerical investigation of transport behaviors of nonspherical proppants in hydraulic fracturing using CFD-DEM. Part. Sci. Technol. 40 (2), 207–218. https://doi.org/10.1080/02726351.2021.1930301.

Tong, S., Mohanty, K., 2017. The effect of connectivity of secondary fractures on proppant placement. In: Proc. 5th Unconv. Resour. Technol. Conf, Austin, Texas. https://doi.org/10.15530/urtec-2017-2671549.

Wang, J., Joseph, D.D., Patankar, N.A., et al., 2003. Bi-power law correlations for sediment transport in pressure driven channel flows. Int. J. Multiphas. Flow 29 (3), 475–494. https://doi.org/10.1016/S0301-9322(02)00152-0.

Wang, X., Yao, J., Gong, L., et al., 2019. Numerical simulations of proppant deposition and transport characteristics in hydraulic fractures and fracture networks. J. Petrol. Sci. Eng. 183, 106401. https://doi.org/10.1016/j.petrol.2019.106401.

Wen, Z., Zhang, L., Tang, H., et al., 2022. A review on numerical simulation of proppant transport: Eulerian–Lagrangian views. J. Petrol. Sci. Eng. 217, 110902.

https://doi.org/10.1016/j.petrol.2022.110902.
Xie, H.P., 1995. Fractal description of rock joints. Chin. J. Geotech. Eng. 1, 18–23.
Xu, J., Ding, Y., Yang, L., et al., 2021. Conductivity analysis of tortuous fractures filled with non-spherical proppants. J. Petrol. Sci. Eng. 198 (B2), 108235. https://doi.org/10.1016/j.petrol.2020.108235.
Zeng, J.S., Li, H., Zhang, D.X., 2016. Numerical simulation of proppant transport in hydraulic fracture with the upscaling CFD-DEM method. J. Nat. Gas Sci. Eng. 33, 264–277. https://doi.org/10.1016/j.jngse.2016.05.030.
Zhang, A., Yang, J., Cheng, L., Ma, C., 2022. A simulation study on stress-seepage characteristics of 3D rough single fracture based on fluid-structure interaction. J. Pet. Sci. Eng. 211, 110215. https://doi.org/10.1016/j.petrol.2022.110215.
Zhao, K., Wang, J., Xu, H., Zhang, L., et al., 2023. Numerical simulation of proppant migration and sedimentation behavior in complex fractures based on computational fluid dynamics. Phys. Fluids 35 (9), 093103. https://doi.org/10.1063/5.0167046.
Zhou, H., Mo, G., Zhao, J., Cen, K., 2011. DEM–CFD simulation of the particle dispersion in a gas–solid two-phase flow for a fuel-rich/lean burner. Fuel 90 (4), 1584–1590. https://doi.org/10.1016/j.fuel.2010.10.017.
Zhou, H.W., Xie, H., 2003. Direct estimation of the fractal dimensions of a fracture surface of rock. Surf. Rev. Lett. 10 (5), 751–762. https://doi.org/10.1142/S0218625X03005591.

Nomenclature

CFD-DEM: Computational Fluid Dynamics-Discrete Element Method
t: time, s
$\boldsymbol{u}$: fluid velocity, m/s
p: pressure of the fluid, Pa
S_f: average interaction force per unit volume, N
M: number of particles in the cell
$\boldsymbol{F}_{f,i}$: fluid force on the particles, N
V_{cell}: volume of fluid in the calculated cell
S_p: sphericity of the particle
d_n: diameter of the equivalent volume of the sphere, m
d_c: diameter of external sphere, m
m_p: mass of particle p, kg
$\boldsymbol{F}_{c,i}^{p}$: contact force acting on particle p, N
k_c: number of spherical elements on the external surface
$\boldsymbol{F}_D$: fluid drag force, N
$\boldsymbol{F}_M$: magnus force, N
$\boldsymbol{F}_S$: Saffman lift, N
$\boldsymbol{F}_p$: fluid pressure gradient force, N
$\boldsymbol{T}_{t,e}^{p}$: tangential torque vector, N·m
$\boldsymbol{T}_{r,e}^{p}$: normal torque vector, N·m
$\boldsymbol{I}_p$: the moment of inertia, kg·m^2
E^*: equivalent Young's modulus, Pa
Re_r: Reynolds number
$\boldsymbol{T}_{DT}^{p}$: drag torque generated by rotation, N·m
$\boldsymbol{F}_{n,ij}^{n}$: normal contact force, N
$\boldsymbol{F}_{n,ij}^{d}$: normal damping force, N
R^*: equivalence radius, m
m^*: the equivalent particle mass, kg
$\boldsymbol{S}_{n,ij}$: normal stiffness, N/m
$\boldsymbol{v}_{n,pq}$: relative normal velocity component of the contact point, m/s
e: recovery factor
G^*: equivalent shear modulus, Pa
$\boldsymbol{v}_{t,pq}$: relative tangential velocity at the contact point, m/s
$\boldsymbol{F}_{t,ij}^{n}$: tangential contact force, N
$\boldsymbol{F}_{t,ij}^{d}$: tangential damping force, N
$\boldsymbol{u}_f - \boldsymbol{u}_p$: slip velocity, m/s
A_P: frontal area of the particle, m^2
C_D: coefficient of drag
C_{DR}: rotational drag coefficient
C_{LS}: lift coefficient
d_p: diameter of the particle, m
$\frac{dp}{dx}$: pressure gradient along the x direction
JRC: Joint Roughness Coefficient
$C_h(u,v)$: the auto-correlation function
u, v: the lag along x, y directions, respectively
l_{c1}, l_{c2}: correlation length coefficients in the x, y direction
μ_s: sliding friction coefficient
α: volume fraction of the fluid phase
ρ_f: fluid density, kg/m^3
ρ_p: density of particle p, kg/m^3
$\boldsymbol{\tau}$: viscous stress tensor, N/m^2
$\boldsymbol{\delta}_{n,ij}$: normal overlap of the particles
$\boldsymbol{\Omega}$: angular velocity of particle relative to the fluid, rad/s
ε: function of the effect of other particles
$\boldsymbol{\omega}_f$: rotational velocity of the fluid, rad/s
$\boldsymbol{\omega}_p$: angular velocity of the particle, rad/s
σ_h^2: the square of the overall roughness